

Singlet Dirac Fermion Dark Matter with Mediators at Loop

Junji Hisano^{a,b,c}, Ryo Nagai^d, and Natsumi Nagata^e

^a*Kobayashi-Maskawa Institute for the Origin of Particles and the Universe,
Nagoya University, Nagoya 464-8602, Japan*

^b*Department of Physics, Nagoya University, Nagoya 464-8602, Japan*

^c*Kavli IPMU (WPI), UTIAS, University of Tokyo, Kashiwa, Chiba 277-8583, Japan*

^d*Department of Physics, Tohoku University, Sendai, Miyagi 980-8578, Japan*

^e*Department of Physics, University of Tokyo, Bunkyo-ku, Tokyo 113-0033, Japan*

Abstract

We study the phenomenology of singlet Dirac fermion dark matter in the simplified models where the dark matter interacts with the Standard Model particles at loop-level with the help of either colored or non-colored mediators. We especially focus on the implications of non-zero CP phases in the dark sector, which induce the electric dipole moments of the Dirac fermion dark matter as well as those of electron and nucleon. It is then found that the dark matter direct detection searches and the measurements of the electric dipole moments are able to test the singlet Dirac fermion dark matter scenario in the forthcoming experiments.

1 Introduction

Weakly-interacting massive particles (WIMPs) offer the most promising framework to explain dark matter (DM) in the Universe, as their thermal relic abundance naturally agrees with the observed DM density. A variety of possibilities for WIMP DM candidates have been proposed and studied so far [1]; for instance, a real or complex scalar particle that is singlet under the Standard Model (SM) gauge interactions and is stabilized by, *e.g.*, a \mathbb{Z}_2 symmetry is known to be the simplest example for WIMP DM [2]. This scalar DM has a quartic coupling with the SM Higgs field at the renormalizable level, which allows the DM particles to annihilate into SM particles. This DM interacts with nucleons through this quartic coupling, which enables us to test this DM model in future DM direct detection experiments.

Fermionic DM candidates are, on the other hand, classified into either a Majorana or Dirac fermion. It turns out that these two classes of DM candidates have different phenomenological properties, as Majorana fermions have neither vector nor dipole interactions, while Dirac fermions are able to have both of those interactions. In addition, pair annihilation cross sections of Majorana fermions into light fermions are suppressed as the *s*-wave annihilation requires chirality flip, while those of Dirac fermions are free from such suppression. Thus, for Dirac fermion DM, heavier mass regions may be favored in terms of the thermal relic abundance compared to Majorana fermion DM, which allows a simple explanation for the null results in the existing DM searches such as the LHC and DM direct detection experiments.

In this paper, we focus on the singlet Dirac fermion DM. If DM is a Dirac fermion, there should exist a U(1) symmetry, either global or gauged, under which the DM has a non-zero charge so that the nature of Dirac fermion is maintained. This possibility is theoretically interesting since it explains the stability of the DM as in the case of proton, which is cosmologically stable because of an accidental global U(1) symmetry (baryon number) in the SM. Such a setup is also motivated by the so-called asymmetric DM scenario [3], in which asymmetry in the DM particle and antiparticle number densities accounts for the observed DM density.

When DM is a fermion which is singlet under the SM gauge interactions, additional fields called mediators are required in order for the DM to interact with the SM sector. This is because there is no renormalizable interaction of the DM with the SM fields. A variety of options for introducing such mediators have been considered so far. A simple way is to add a singlet scalar particle which couples to both the fermionic DM and the SM Higgs boson [4]. Another way is to assume that DM couples to a neutral gauge boson which interacts with the SM fields as well [5, 6]. Moreover, if there are extra scalars that have the same quantum numbers as those of the SM fermions, DM may couple to the SM fermions directly with the help of these scalar particles [7–9]. If one introduces an $SU(2)_L$ doublet fermion with hypercharge $\pm 1/2$, we may also couple the singlet fermion DM to the SM Higgs field.

In all of the above cases, the fermionic DM couples to the SM sector at tree level. On the other hand, in this paper, we study the cases where the Dirac fermion DM does not

couple to the SM sector at tree level, but does couple to it at loop level. To that end, we consider simplified Dirac fermion DM models, where extra fermions and scalars with non-zero SM gauge charges are coupled with the Dirac fermion DM.¹ As mentioned above, the Dirac fermion DM may have vector and tensor couplings, which considerably affect the direct detection rate of DM. However, the significance of these couplings depends on models. For instance, if the Dirac fermion DM had a direct coupling with light quarks via a mediator, this interaction would induce vector-current four-Fermi interactions with light quarks at tree level after the mediator is integrated out, but such interactions cause a large DM-nucleus scattering cross section and thus have already been severely constrained by the DM direct detection experiments. If, on the other hand, the Dirac fermion DM is coupled to the SM sector at loop level, these vector interactions are suppressed by a loop factor and the direct detection bound may be evaded. It turns out that in this case the tensor couplings may give significant contributions to the DM direct detection even if they are also suppressed by one-loop factor. The Dirac fermion DM may have a magnetic dipole moment (MDM)—and an electric dipole moment (EDM) as well if the DM-mediator interactions contain CP phases. These dipole moments open up possibilities to test this DM candidate in DM direct detection experiments [11].

As it turns out, the detectability of the DM through the dipole moments is considerably affected by the size of the EDM, which depends on the CP phases in the DM-mediator couplings. These CP phases, as well as the CP phases in the mediator-Higgs couplings, also induce CP-odd quantities in the SM sector at loop level, and thus we may probe them through the measurements of electron and nucleon EDMs. In particular, if the Dirac fermion DM is accompanied with colored mediators, they generate the dimension-six Weinberg operator [12], which then induces nucleon EDMs. We thus expect a close correlation between the DM and nucleon EDMs, which has significant implications for the testability of this DM scenario in the future DM direct detection and EDM experiments.

This paper is organized as follows. In the next section, we show our simplified Dirac fermion DM models. We then briefly discuss the thermal relic abundance of DM in the models in Sec. 3. The DM direct detection and the electron and nucleon EDMs generated in these model are discussed in Sec. 4 and Sec. 5, respectively. Then, in Sec. 6, we show the current constraints on our simplified Dirac fermion DM models, and discuss their testability in future experiments. Section 7 is devoted to conclusion and discussion.

2 Simplified Dirac Fermion DM Models

2.1 Field content and Lagrangian

To begin with, we show our simplified Dirac fermion DM models which we discuss in this paper. The Dirac fermion DM χ is composed of two Weyl fermions, ξ_χ and η_χ , which

¹See also Ref. [10] for a relevant work, where the Dirac fermion DM is supposed to interact with the SM sector at loop level through non-colored mediators. In this paper, we also consider colored mediators, which give rise to rich phenomenology as we see below.

Table 1: Quantum numbers of DM and mediators. A new global symmetry $U(1)_D$ is for stability of the DM.

Field	Spin	$SU(3)_C$	$SU(2)_L$	$U(1)_Y$	$U(1)_D$
ξ_X	1/2	1	1	0	+1
η_X	1/2	1	1	0	-1
ξ_Q	1/2	3	2	$\frac{1}{6}$	0
η_Q	1/2	$\bar{\mathbf{3}}$	2	$-\frac{1}{6}$	0
\tilde{Q}	0	3	2	$\frac{1}{6}$	+1
$\xi_{\bar{u}}$	1/2	$\bar{\mathbf{3}}$	1	$-\frac{2}{3}$	0
$\eta_{\bar{u}}$	1/2	3	1	$\frac{2}{3}$	0
\tilde{u}	0	$\bar{\mathbf{3}}$	1	$-\frac{2}{3}$	-1
$\xi_{\bar{d}}$	1/2	$\bar{\mathbf{3}}$	1	$\frac{1}{3}$	0
$\eta_{\bar{d}}$	1/2	3	1	$-\frac{1}{3}$	0
\tilde{d}	0	$\bar{\mathbf{3}}$	1	$\frac{1}{3}$	-1
ξ_L	1/2	1	2	$-\frac{1}{2}$	0
η_L	1/2	1	2	$\frac{1}{2}$	0
\tilde{L}	0	1	2	$-\frac{1}{2}$	+1
$\xi_{\bar{e}}$	1/2	1	1	1	0
$\eta_{\bar{e}}$	1/2	1	1	-1	0
\tilde{e}	0	1	1	1	-1

are assumed to be singlet under the SM gauge interactions.² We then introduce a global $U(1)$ symmetry, $U(1)_D$, and assume that these fermions have the $U(1)_D$ charge +1 and -1, respectively. The SM particles are supposed to be singlet under the $U(1)_D$ symmetry.

In addition, we introduce vector-like fermions and complex scalars as mediators, in order to couple the Dirac fermion DM to the SM sector at loop level. These additional particles have SM gauge interactions, which then induce the couplings of the DM with the SM gauge bosons through quantum corrections. To avoid stable charged/colored fermions, we assume the extra vector-like fermions to have the same quantum numbers as those of the SM fermions and to mix with the SM fermions by a small amount. Thus, these extra fermions should be singlet under $U(1)_D$. For the DM to couple with the extra fermions, we need to assume that the extra scalar particles also have the same quantum numbers as those of the SM fermions and are charged under $U(1)_D$. These $U(1)_D$ -charged

²Weyl fermions are assumed to be left-handed throughout this paper.

scalars are supposed to be heavier than the Dirac fermion DM to insure the stability of DM.

We list sets of such extra scalars and fermions and show their quantum numbers in Table 1. Here, all of the fermionic fields are introduced in a vector-like manner so that they form Dirac fields. This simultaneously assures that these new fermions do not cause gauge anomaly. In addition, since the Dirac fermion DM is the only fermion that has non-zero $U(1)_D$ charge, this $U(1)_D$ symmetry is also anomaly-free.³

In what follows, we consider two models where different sets of fields are added to the SM besides the Dirac fermion DM χ ; Model I contains $\xi_Q, \eta_Q, \tilde{Q}, \xi_{\bar{u}}, \eta_{\bar{u}}, \tilde{u}, \xi_{\bar{d}}, \eta_{\bar{d}}$, and \tilde{d} , while Model II includes $\xi_L, \eta_L, \tilde{L}, \xi_{\bar{e}}, \eta_{\bar{e}}$, and \tilde{e} . These sets of particles are shaded in pink and green in Table 1, respectively. These two models are qualitatively different, since in Model I the DM interacts with colored particles while it does not in Model II. We also denote the $SU(2)_L$ component fields of ξ_Q, η_Q, ξ_L , and η_L by

$$\xi_Q = \begin{pmatrix} \xi_u \\ \xi_d \end{pmatrix}, \quad \eta_Q = \begin{pmatrix} \eta_u \\ \eta_d \end{pmatrix}, \quad \xi_L = \begin{pmatrix} \xi_\nu \\ \xi_e \end{pmatrix}, \quad \eta_L = \begin{pmatrix} \eta_\nu \\ \eta_e \end{pmatrix}, \quad (1)$$

respectively, while for \tilde{Q} and \tilde{L}

$$\tilde{Q} = \begin{pmatrix} \tilde{u} \\ \tilde{d} \end{pmatrix}, \quad \tilde{L} = \begin{pmatrix} \tilde{\nu} \\ \tilde{e} \end{pmatrix}. \quad (2)$$

The mass terms of these fields are given by

$$\mathcal{L}_{\text{mass}} = - \left[\mu_\chi \xi_\chi \eta_\chi + \sum_f \mu_f \xi_f \eta_f + \text{h.c.} \right] - \sum_f \tilde{m}_f^2 |\tilde{f}|^2, \quad (3)$$

where the sum is taken over the extra matters in each model. \tilde{m}_f^2 are real, while μ_χ and μ_f are in general complex quantities.

In both of the models, the Dirac fermion DM has the following interactions:

$$\begin{aligned} \mathcal{L}_{\chi f \tilde{f}} = & a_Q \xi_\chi \xi_Q \tilde{Q}^* + b_Q \eta_\chi \eta_Q \tilde{Q} + a_{\bar{u}} \xi_\chi \eta_{\bar{u}} \tilde{u} + b_{\bar{u}} \eta_\chi \xi_{\bar{u}} \tilde{u}^* + a_{\bar{d}} \xi_\chi \eta_{\bar{d}} \tilde{d} + b_{\bar{d}} \eta_\chi \xi_{\bar{d}} \tilde{d}^* \\ & + a_L \xi_\chi \xi_L \tilde{L}^* + b_L \eta_\chi \eta_L \tilde{L} + a_{\bar{e}} \xi_\chi \eta_{\bar{e}} \tilde{e} + b_{\bar{e}} \eta_\chi \xi_{\bar{e}} \tilde{e}^* + \text{h.c.} . \end{aligned} \quad (4)$$

These interactions induce the annihilation of the DM into the extra vector-like fermions via t -channel exchange of the extra scalars if the vector-like fermions are lighter than the DM.

³For this reason, we may also consider the gauged $U(1)_D$ symmetry instead of the global symmetry. In this case, the Dirac fermion DM has the $U(1)_D$ gauge interaction, which may affect its phenomenological properties significantly. Although this is an interesting possibility, we do not consider this case in the following discussion.

The vector-like fermions may have Yukawa couplings with the SM Higgs field H as they are allowed by the gauge invariance in the models,

$$\begin{aligned} \mathcal{L}_{\text{Yukawa}} = & -\kappa_{\tilde{u}}\xi_{\tilde{u}}\epsilon_{\alpha\beta}(\xi_Q)_\alpha(H)_\beta - \kappa'_{\tilde{u}}\eta_{\tilde{u}}(\eta_Q)^\alpha(\tilde{H})_\alpha \\ & -\kappa_{\tilde{d}}\xi_{\tilde{d}}(\xi_Q)_\alpha(H^\dagger)^\alpha - \kappa'_{\tilde{d}}\eta_{\tilde{d}}(\eta_Q)^\alpha(H)_\alpha \\ & -\kappa_{\tilde{e}}\xi_{\tilde{e}}(\xi_L)_\alpha(H^\dagger)^\alpha - \kappa'_{\tilde{e}}\eta_{\tilde{e}}(\eta_L)^\alpha(H)_\alpha + \text{h.c.} , \end{aligned} \quad (5)$$

where α, β are $\text{SU}(2)_L$ indices, $\epsilon_{\alpha\beta}$ is the anti-symmetric tensor with $\epsilon_{12} = -\epsilon_{21} = +1$, and $\tilde{H} \equiv i\tau_2 H^\dagger$. Note that, in this paper, we have defined η_Q and η_L such that they transform as anti-fundamental representations of $\text{SU}(2)_L$; *i.e.*, $i\tau_2\eta_Q$ and $i\tau_2\eta_L$ are fundamental representations of $\text{SU}(2)_L$, where τ_a ($a = 1, 2, 3$) are the Pauli matrices. As mentioned above, we assume that the extra vector-like fermions have small but non-zero Yukawa couplings with the SM fermions so that these vector-like fermions decay into the SM fermions;⁴ we do not show these terms explicitly here and hereafter. The new scalar fields may also have trilinear terms similar to the terms in Eq. (5):

$$\mathcal{L}_{\text{tri}} = -A_{\tilde{u}}\tilde{u}\epsilon_{\alpha\beta}(\tilde{Q})_\alpha(H)_\beta - A_{\tilde{d}}\tilde{d}(\tilde{Q})_\alpha(H^\dagger)^\alpha - A_{\tilde{e}}\tilde{e}(\tilde{L})_\alpha(H^\dagger)^\alpha + \text{h.c.} . \quad (6)$$

In addition, there may be quartic couplings

$$\mathcal{L}_{\text{quart}} = -\sum_f \lambda_f |\tilde{f}|^2 |H|^2 - \lambda'_Q \tilde{Q}^\dagger \tau_a \tilde{Q} H^\dagger \tau_a H - \lambda'_L \tilde{L}^\dagger \tau_a \tilde{L} H^\dagger \tau_a H + \dots , \quad (7)$$

where dots indicate other quartic terms that contain only the new scalar fields. Such terms are irrelevant to the following analysis, and thus we neglect them in what follows. The extra-scalar interactions in Eqs. (6) and (7) give rise to the mass terms of the extra scalars as we see in the next subsection.

2.2 Mass eigenstates

After the Higgs field develops a vacuum expectation value (VEV),⁵

$$\langle H \rangle = \frac{1}{\sqrt{2}} \begin{pmatrix} 0 \\ v \end{pmatrix} , \quad (8)$$

with $v \simeq 246$ GeV, the extra fermions and scalars mix among each other. For the fermionic part, the mass terms are

$$\mathcal{L}_{\text{mass}}^{(\text{ferm})} = -\sum_{f=u,d,e} (\eta_f, \xi_{\tilde{f}}) \mathcal{M}_f \begin{pmatrix} \xi_f \\ \eta_{\tilde{f}} \end{pmatrix} - \mu_L \xi_\nu \eta_\nu + \text{h.c.} , \quad (9)$$

⁴The upper limits on the mixing angles between the SM fermions and the vector-like fermions imposed by flavor experiments are $\mathcal{O}(10^{-4})$ in the most stringent cases (see, *e.g.*, Refs. [13–16]); with this size of mixing angles, the vector-like fermions decay almost promptly.

⁵We take v to be real without loss of generality.

where

$$\mathcal{M}_u = \begin{pmatrix} \mu_Q & \frac{v}{\sqrt{2}}\kappa'_{\bar{u}} \\ \frac{v}{\sqrt{2}}\kappa_{\bar{u}} & \mu_{\bar{u}} \end{pmatrix}, \quad \mathcal{M}_d = \begin{pmatrix} \mu_Q & \frac{v}{\sqrt{2}}\kappa'_{\bar{d}} \\ \frac{v}{\sqrt{2}}\kappa_{\bar{d}} & \mu_{\bar{d}} \end{pmatrix}, \quad \mathcal{M}_e = \begin{pmatrix} \mu_L & \frac{v}{\sqrt{2}}\kappa'_{\bar{e}} \\ \frac{v}{\sqrt{2}}\kappa_{\bar{e}} & \mu_{\bar{e}} \end{pmatrix}. \quad (10)$$

Each mass matrix \mathcal{M}_f ($f = u, d, e$) is diagonalized by means of biunitary transformation as

$$V_{fR}^\dagger \mathcal{M}_f V_{fL} = \begin{pmatrix} m_{f_1} & 0 \\ 0 & m_{f_2} \end{pmatrix}, \quad (11)$$

where m_{f_i} ($i = 1, 2$) are real and non-negative, and we denote the corresponding Dirac fermions in the mass eigenbasis by ψ_{f_i} . The relations between the mass eigenstates and the weak eigenstates are given by

$$\begin{pmatrix} \xi_f \\ \eta_{\bar{f}} \end{pmatrix} = V_{fL} \begin{pmatrix} \psi_{f_1L} \\ \psi_{f_2L} \end{pmatrix}, \quad \begin{pmatrix} \eta_f^\dagger \\ \xi_{\bar{f}}^\dagger \end{pmatrix} = V_{fR} \begin{pmatrix} \psi_{f_1R} \\ \psi_{f_2R} \end{pmatrix}, \quad (12)$$

where L (R) represents the left-handed (right-handed) components of ψ_{f_i} . The Dirac mass term for ξ_ν and η_ν is taken to be real and non-negative via an appropriate phase rotation, where the Dirac field is given by

$$\psi_\nu = \begin{pmatrix} e^{\frac{i}{2}\theta_L} \xi_\nu \\ e^{-\frac{i}{2}\theta_L} \eta_\nu^\dagger \end{pmatrix}, \quad (13)$$

with $\theta_L \equiv \arg(\mu_L)$, and its mass is given by $m_\nu = |\mu_L|$. Similarly, by defining the Dirac fermion DM field

$$\chi \equiv \begin{pmatrix} e^{\frac{i}{2}\theta_\chi} \eta_\chi \\ e^{-\frac{i}{2}\theta_\chi} \xi_\chi^\dagger \end{pmatrix}, \quad (14)$$

with $\theta_\chi \equiv \arg(\mu_\chi)$, we have the DM mass term of the form $-m_\chi \bar{\chi} \chi$ with $m_\chi \equiv |\mu_\chi|$.

As we see, the DM fermions ξ_χ and η_χ form a Dirac fermion with an identical mass m_χ . This remains unchanged even if radiative corrections are included. This is because the interaction terms presented in the previous subsection preserve the $U(1)_D$ symmetry, which is not spontaneously broken as the SM Higgs field H is not charged under the $U(1)_D$ symmetry. Since ξ_χ and η_χ are charged under $U(1)_D$, Majorana mass terms for these fields, with which these two fields split into two Majorana fermions, are not generated as long as the $U(1)_D$ symmetry is preserved.

For the scalar fields, on the other hand, the mass terms are written as

$$\mathcal{L}_{\text{mass}}^{(\text{sca})} = - \sum_{f=u,d,e} \left(\tilde{f}^*, \tilde{f} \right) \tilde{\mathcal{M}}_f^2 \begin{pmatrix} \tilde{f} \\ \tilde{f}^* \end{pmatrix} - \tilde{m}_\nu^2 |\tilde{\nu}|^2, \quad (15)$$

where

$$\begin{aligned}\widetilde{\mathcal{M}}_u^2 &= \begin{pmatrix} \widetilde{m}_Q^2 + \frac{\lambda_Q - \lambda'_Q}{2} v^2 & \frac{v}{\sqrt{2}} A_{\bar{u}}^* \\ \frac{v}{\sqrt{2}} A_{\bar{u}} & \widetilde{m}_{\bar{u}}^2 + \frac{\lambda_{\bar{u}}}{2} v^2 \end{pmatrix}, & \widetilde{\mathcal{M}}_d^2 &= \begin{pmatrix} \widetilde{m}_Q^2 + \frac{\lambda_Q + \lambda'_Q}{2} v^2 & \frac{v}{\sqrt{2}} A_{\bar{d}}^* \\ \frac{v}{\sqrt{2}} A_{\bar{d}} & \widetilde{m}_{\bar{d}}^2 + \frac{\lambda_{\bar{d}}}{2} v^2 \end{pmatrix}, \\ \widetilde{\mathcal{M}}_e^2 &= \begin{pmatrix} \widetilde{m}_L^2 + \frac{\lambda_L + \lambda'_L}{2} v^2 & \frac{v}{\sqrt{2}} A_{\bar{e}}^* \\ \frac{v}{\sqrt{2}} A_{\bar{e}} & \widetilde{m}_{\bar{e}}^2 + \frac{\lambda_{\bar{e}}}{2} v^2 \end{pmatrix}, & \widetilde{m}_\nu^2 &= \widetilde{m}_L^2 + \frac{\lambda_L - \lambda'_L}{2} v^2.\end{aligned}\quad (16)$$

The mass matrices $\widetilde{\mathcal{M}}_f^2$ ($f = u, d, e$) are Hermitian, and thus diagonalized by unitary matrices \widetilde{V}_f as

$$\widetilde{V}_f^\dagger \widetilde{\mathcal{M}}_f^2 \widetilde{V}_f = \begin{pmatrix} \widetilde{m}_{f_1}^2 & 0 \\ 0 & \widetilde{m}_{f_2}^2 \end{pmatrix}, \quad (17)$$

with the mass eigenstates given by

$$\begin{pmatrix} \widetilde{f} \\ \widetilde{f}^* \end{pmatrix} = \widetilde{V}_f \begin{pmatrix} \widetilde{f}_1 \\ \widetilde{f}_2 \end{pmatrix}. \quad (18)$$

The interactions of the new particles in the mass eigenbasis are presented in Appendix A.

2.3 CP phases

Many of the couplings newly introduced in our simplified Dirac fermion DM models are in general complex. Field redefinition cannot remove all of the CP phases, and thus the remaining CP phases are physical. These physical CP phases induce the EDM of the Dirac fermion DM as well as those of electron and nucleon. As it turns out, the EDM of the DM significantly affects the DM direct detection rate.

For later use, let us summarize the physical CP phases and express them in a rephasing invariant manner:

$$\varphi_{\mu_f} \equiv \arg(\mu_\chi \mu_f a_f^* b_f^*), \quad (19)$$

for $f = Q, \bar{u}, \bar{d}, L, \bar{e}$, and

$$\varphi_{\kappa_{\bar{f}}} \equiv \arg(\mu_f \mu_{\bar{f}} \kappa_{\bar{f}}^* \kappa_{\bar{f}}'^*), \quad \varphi_{A_{\bar{f}}} \equiv \arg(A_{\bar{f}} \mu_f b_{\bar{f}}^* \kappa_{\bar{f}}^*), \quad (20)$$

for $f = u, d, e$. The combinations $A_{\bar{f}} \mu_f^* a_f^* \kappa_{\bar{f}}'$ are also rephasing invariant though the phases are given by linear combinations of the above phases.

3 Thermal Relic Abundance

The DM couplings in Eq. (4) keep the Dirac fermion DM χ in thermal equilibrium with the SM particles in the early Universe. Once the temperature of the Universe falls down below the DM mass, its number density exponentially decreases, and eventually the annihilation

processes freeze out, and the number of the DM particles in a unit comoving volume becomes constant. The resultant DM relic density is thus determined by only the pair annihilation cross section of the DM particles at the decoupling temperature, unless other particles with nonzero $U(1)_D$ charges are degenerate with the DM particles in mass so that significant amount of these particles is left in the thermal bath at the decoupling temperature.

In the present model, the DM particles annihilate through the couplings in Eq. (4); they annihilate into the vector-like fermions through the t -channel scalar exchange processes if the vector-like fermions are lighter than the Dirac fermion DM. If the vector-like fermions are heavier than the DM, on the other hand, the tree-level annihilation processes into the vector-like fermions are kinematically forbidden and they annihilate into the SM particles at loop level; therefore, in this case the annihilation cross section is much smaller than the former case. To obtain a sizable annihilation cross section, we assume throughout this work that the vector-like fermions are lighter than the Dirac fermion DM, though we may find a parameter region in which the correct relic abundance is obtained even when the DM particle is lighter than the vector-like fermions.

The Dirac fermion and its antiparticle annihilate efficiently via s -wave annihilation processes. Expanding in powers of the relative velocity between these particles, v_{rel} , and keeping only the leading contribution, we obtain the cross section of the annihilation process $\chi\bar{\chi} \rightarrow \psi_{f_i}\bar{\psi}_{f_j}$, $\sigma_{\text{ann}}^{(i,j)}$, as

$$\begin{aligned}
\sigma_{\text{ann}}^{(i,j)} v_{\text{rel}} &\simeq \frac{N_c m_\chi^2}{32\pi} \left[1 - \frac{m_{f_i}^2 + m_{f_j}^2}{2m_\chi^2} + \frac{(m_{f_i}^2 - m_{f_j}^2)^2}{16m_\chi^4} \right]^{\frac{1}{2}} \\
&\times \sum_{k,l} \frac{1}{[\tilde{m}_{f_k}^2 + m_\chi^2 - \frac{1}{2}(m_{f_i}^2 + m_{f_j}^2)][\tilde{m}_{f_l}^2 + m_\chi^2 - \frac{1}{2}(m_{f_i}^2 + m_{f_j}^2)]} \\
&\times \left[(C_{f_\chi L}^{*ik} C_{f_\chi L}^{il} + C_{f_\chi R}^{*ik} C_{f_\chi R}^{il}) \left(1 + \frac{m_{f_i}^2 - m_{f_j}^2}{4m_\chi^2} \right) + (C_{f_\chi R}^{*ik} C_{f_\chi L}^{il} + C_{f_\chi L}^{*ik} C_{f_\chi R}^{il}) \frac{m_{f_i}}{m_\chi} \right] \\
&\times \left[(C_{f_\chi L}^{*jl} C_{f_\chi L}^{jk} + C_{f_\chi R}^{*jl} C_{f_\chi R}^{jk}) \left(1 - \frac{m_{f_i}^2 - m_{f_j}^2}{4m_\chi^2} \right) + (C_{f_\chi R}^{*jl} C_{f_\chi L}^{jk} + C_{f_\chi L}^{*jl} C_{f_\chi R}^{jk}) \frac{m_{f_j}}{m_\chi} \right],
\end{aligned} \tag{21}$$

where $N_c = 3$ (1) for vector-like quark (lepton) final states. The couplings $C_{f_\chi L/R}^{ik}$ are given in Appendix A.3. Notice that this s -wave contribution remains sizable even if the DM couplings are purely chiral (either $C_{f_\chi R}^{ik}$ or $C_{f_\chi L}^{ik}$ vanishes) and the final state fermions are massless ($m_{f_i} = 0$), contrary to the case of Majorana fermion DM.

To roughly estimate the typical size of the annihilation cross section, we take $a_f =$

$a_{\bar{f}} = a$, $b_f = b_{\bar{f}} = \kappa_{\bar{f}} = \kappa'_{\bar{f}} = A_{\bar{f}} = \theta_\chi = 0$, $m_{f_i} = m_f$, and $\tilde{m}_{f_i} = \tilde{m}_f$. We then have

$$\begin{aligned} \sigma_{\text{ann}} v_{\text{rel}} &\simeq \frac{N_c |a|^4}{32\pi} \left[1 - \frac{m_f^2}{m_\chi^2} \right]^{\frac{1}{2}} \frac{m_\chi^2}{[\tilde{m}_f^2 + m_\chi^2 - m_f^2]^2} \\ &\simeq N_c |a|^4 \left[1 - \frac{m_f^2}{m_\chi^2} \right]^{\frac{1}{2}} \left(\frac{m_\chi}{1 \text{ TeV}} \right)^2 \left(\frac{1 \text{ TeV}^2}{\tilde{m}_f^2 + m_\chi^2 - m_f^2} \right)^{-2} \times 10^{-25} \text{ cm}^3/\text{s} , \end{aligned} \quad (22)$$

for each vector-like fermion. It is known that the thermal relic abundance of Dirac fermion DM reproduces the observed value of the DM density, $\Omega_{\text{DM}} h^2 \simeq 0.12$ [17], if its thermal-averaged annihilation cross section is $\simeq 2 \times (2 - 3) \times 10^{-26} \text{ cm}^3/\text{s}$, where the factor of two is included as both DM fermion and anti-fermion contribute to the relic density. This simple estimation shows that the thermal relic abundance of the singlet Dirac fermion DM agrees to the correct DM density if the DM, vector-like fermions, and new scalars lie around the TeV scale and the relevant couplings are $\mathcal{O}(1)$, which we confirm below.

In principle, one could require the condition that the thermal relic abundance of the Dirac fermion DM should reproduce $\Omega_{\text{DM}} h^2 \simeq 0.12$ [17] so that a parameter in this model is fixed as a function of the other parameters, and make predictions for other observables with this constraint imposed. It turns out, however, that this restriction is not so much instructive; first and foremost, the present model has many free parameters and this constraint does not improve the predictivity of this model so much. Second, if the scalar particles are degenerate with the DM in mass (with $\lesssim 10\%$ mass degeneracy), the thermal relic abundance significantly decreases because of the coannihilation effects [18], while other observables are rather insensitive to this degeneracy. In particular, when the colored scalars are degenerate in mass with the DM, the Sommerfeld effect [19–21] and bound-state effect [22, 23] due to QCD interactions significantly reduce the relic abundance. This again spoils a tight correlation between the DM relic density and other observables. Moreover, the Dirac fermion DM accommodates various possibilities that affect its relic abundance, such as the asymmetric DM scenario [3], the presence of extra light U(1) gauge bosons and/or singlet scalar fields, and so on. In most of the cases, these new possibilities have little effect on the detectability of the DM, while the regions favored by thermal relic abundance are considerably changed. For these reasons, in the following analyses, we do not strictly impose the relic abundance condition; we regard all variables in our model as free parameters and show the parameter region favored by the thermal relic abundance just for reference. We however note in passing that we assume the standard cosmological history in our calculations of the DM relic abundance—deviations from the standard picture, such as the late-time entropy production after the DM freeze-out, may also affect the DM relic abundance significantly.

4 Direct Detection

In our simplified Dirac fermion DM models, the singlet Dirac fermion DM couples with the SM particles through the radiative corrections. Thus, the DM candidate may be tested in

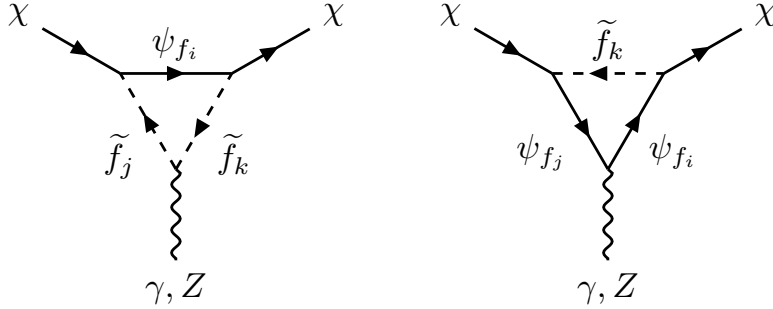


Figure 1: Feynman diagrams for effective DM- γ/Z interactions.

direct DM searches. In this section, we calculate the relevant effective interactions of the DM with SM fields, and then evaluate the expected event rates in DM direct detection experiments.

4.1 Effective interactions

To begin with, let us consider the effective couplings of DM with photon (γ). The Dirac fermion DM couples with photon at one-loop level through the Feynman diagrams depicted in Fig. 1. The relevant DM- γ interactions for the direct detection experiments are given by

$$\mathcal{L}_{\text{eff-}\gamma} = \frac{1}{2}C_M^\gamma \bar{\chi} \sigma^{\mu\nu} \chi F_{\mu\nu} - \frac{i}{2}C_E^\gamma \bar{\chi} \sigma^{\mu\nu} \gamma_5 \chi F_{\mu\nu} + C_R^\gamma \bar{\chi} \gamma^\mu \chi \partial^\nu F_{\mu\nu}, \quad (23)$$

with $F_{\mu\nu}$ being the field strength of the photon field, A_μ : $F_{\mu\nu} \equiv \partial_\mu A_\nu - \partial_\nu A_\mu$. Here C_M^γ , C_E^γ , and C_R^γ denote the Wilson coefficients for the DM magnetic dipole moment (DM-MDM), the DM electric dipole moment (DM-EDM), and the DM charge radius (DM-CR), respectively. These Wilson coefficients are obtained through the matching of our models onto the effective theory with these interactions; the concrete expressions for these Wilson coefficients are summarized in Appendix B.1. The DM-EDM is induced in the presence of non-zero CP-phases in the DM-mediator couplings. We note in passing that we have ignored the DM anapole moment, described by the effective operator $\bar{\chi} \gamma^\mu \gamma_5 \chi \partial^\nu F_{\mu\nu}$, as this contribution is always subdominant due to the velocity suppression.

As we see in Sec. 2, there are many free parameters in both Model I and II. To simplify the analysis, in what follows, we focus on the following five cases and study their phenomenologies:

- Model I-A: Model I with $a_Q = a_{\bar{u}} = a_{\bar{d}} \equiv a$ and $b_Q = b_{\bar{u}} = b_{\bar{d}} \equiv b$.
- Model I-B: Model I with $a_Q = a_{\bar{d}} = b_Q = b_{\bar{d}} = 0$, $a_{\bar{u}} \equiv a$, and $b_{\bar{u}} \equiv b$.
- Model I-C: Model I with $a_Q = a_{\bar{u}} = b_Q = b_{\bar{u}} = 0$, $a_{\bar{d}} \equiv a$, and $b_{\bar{d}} \equiv b$.
- Model II-A: Model II with $a_L = a_{\bar{e}} \equiv a$ and $b_L = b_{\bar{e}} \equiv b$.

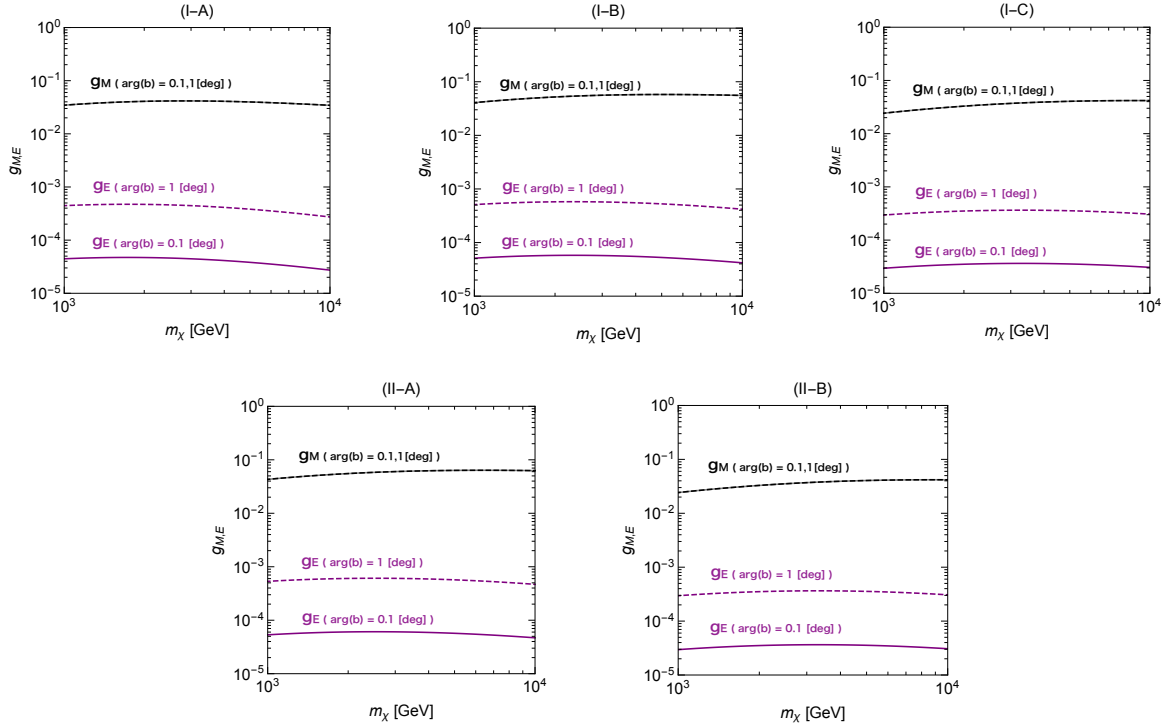


Figure 2: DM-MDM and DM-EDM, g_M and g_E , as functions of DM mass m_χ in the black and purple lines, respectively. We take $a = |b| = 1$, $\lambda'_Q = \lambda'_L = 0$, $\lambda_f = \kappa_{\bar{f}} = \kappa'_{\bar{f}} = 0.5$, $\mu_Q = \mu_L = 800$ GeV, $\mu_{\bar{u}} = 750$ GeV, $\mu_{\bar{d}} = \mu_{\bar{e}} = 700$ GeV, while $\tilde{m}_Q = \tilde{m}_L = 1.2M$, $\tilde{m}_{\bar{u}} = 1.1M$, $\tilde{m}_{\bar{d}} = \tilde{m}_{\bar{e}} = M$, and $A_{\bar{f}} = 2M$ ($M = 1.1m_\chi$). The solid and dashed lines correspond to $\arg(b) = 0.1$ and 1 degrees, respectively.

- Model II-B: Model II with $b_L = a_L = 0$, $a_{\bar{e}} \equiv a$, and $b_{\bar{e}} \equiv b$.

The rest of the parameters are set to be certain appropriate values in each analysis.

In Fig. 2, we show the values of the DM-MDM and DM-EDM as functions of the DM mass m_χ in the black and purple lines, respectively, where the Wilson coefficients are normalized such that

$$C_M^\gamma \equiv \frac{eg_M}{4m_\chi}, \quad C_E^\gamma \equiv \frac{eg_E}{4m_\chi}. \quad (24)$$

In all of these plots we take $a = |b| = 1$, $\lambda'_Q = \lambda'_L = 0$, $\lambda_f = \kappa_{\bar{f}} = \kappa'_{\bar{f}} = 0.5$, $\mu_Q = \mu_L = 800$ GeV, $\mu_{\bar{u}} = 750$ GeV, $\mu_{\bar{d}} = \mu_{\bar{e}} = 700$ GeV, while $\tilde{m}_Q = \tilde{m}_L = 1.2M$, $\tilde{m}_{\bar{u}} = 1.1M$, $\tilde{m}_{\bar{d}} = \tilde{m}_{\bar{e}} = M$, and $A_{\bar{f}} = 2M$ ($M = 1.1m_\chi$).⁶ The solid and dashed lines correspond to

⁶ Let us give some comments on the present LHC bounds on the masses of the extra scalars and fermions. For vector-like quarks, the limits strongly depend on their decay modes. If they decay into third-generation quarks, the present limits on the masses are as strong as $\gtrsim 1.3$ TeV [24, 25]. If, on the other hand, they can decay into only the light quarks, the limits can be lower than 500 GeV, depending on their decay channels [26, 27]. For colored scalars, we refer to squark searches; for a DM mass of $\gtrsim 1$ TeV, colored scalars evade the LHC limits as long as their masses are larger than the DM mass [28, 29]. The

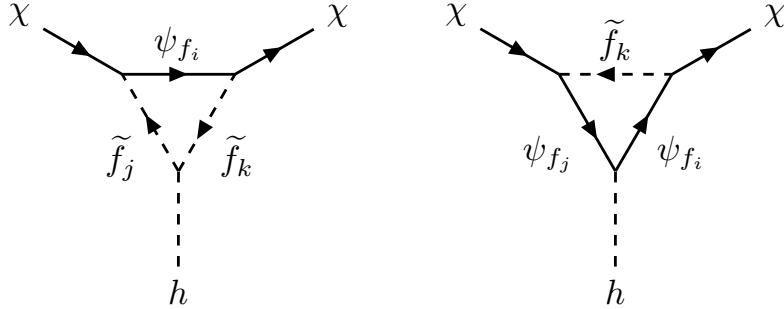


Figure 3: Feynman diagrams for effective DM-Higgs interactions.

$\arg(b) = 0.1$ and 1 degrees, respectively. These plots show that both DM-MDM and EDM described by g_M and g_E , respectively, have little dependence on the DM mass, as we fix the ratios between the DM mass and the scalar masses. In addition, the DM-MDM is almost independent of the CP phases in the DM-mediator couplings, while the DM-EDM strongly depends on these phases as expected.

At one-loop level, the DM- Z boson, DM-Higgs boson, and DM-gluon interactions are also induced through the diagrams shown in Fig. 1, Fig. 3, and Fig. 4, respectively. Explicit formulae for these effective interactions are given in Appendix B.2, B.3, and B.4, respectively. In what follows, we focus on the spin-independent interactions since the limits on these interactions from the direct detection experiments are much stronger than those on the spin-dependent interactions. We also neglect the effective interactions that are suppressed in the non-relativistic limit.

We further integrate out the Z and Higgs bosons to obtain the effective DM-quark/gluon operators. At low energies with three flavor quarks, the relevant interactions are⁷

$$\mathcal{L}_{\text{eff-}q/g} = C_V^q \bar{\chi} \gamma^\mu \chi \bar{q} \gamma_\mu q + C_S^q m_q \bar{\chi} \chi \bar{q} q + C_S^g \bar{\chi} \chi \cdot \frac{\alpha_s}{\pi} G_{\mu\nu}^A G^{A\mu\nu}, \quad (25)$$

where m_q are the quark masses, $\alpha_s \equiv g_s^2/(4\pi)$ with g_s the strong gauge coupling constant, and $G_{\mu\nu}^A$ is the gluon field strength tensor. The vector and scalar couplings C_V^q and C_S^q are generated via the Z and Higgs boson exchange processes, respectively, while the gluonic interaction is induced by the Higgs exchange as well as the vector-like quark loop diagrams shown in Fig. 4. The Wilson coefficients of these operators are given in Appendix B.5.

bounds on non-colored vector-like fermions and scalars are much weaker than those on colored particles. Taking account of these limits, in our analysis, we set the vector-like fermion masses to be $\gtrsim 700$ GeV and the scalar masses to be $> m_\chi \geq 1$ TeV.

⁷We include the factor α_s/π in the definition of the gluon scalar operator such that it is invariant under the renormalization group (RG) flow at one-loop level [30, 31]. This operator runs and mixes with the quark scalar operators at higher orders in α_s , while the vector operator is invariant under the RG flow.

If we turn on the electroweak (EW) radiative corrections, the vector operator mixes with other operators which we have not shown here [32–35]. For example, the $\bar{\chi} \gamma^\mu \chi \bar{q} \gamma_\mu \gamma_5 \chi$ effective interaction induces the vector operator through the EW RG effect, which is order $\frac{y_f^2}{\pi^2} \ln(v/m_{\text{med}}) \sim \mathcal{O}(10\%)$. It is however found that such contributions rarely affect the resultant scattering cross section since the contribution of the vector operator is always subdominant, as we see in Fig. 5. We thus ignore such effects in our analysis.

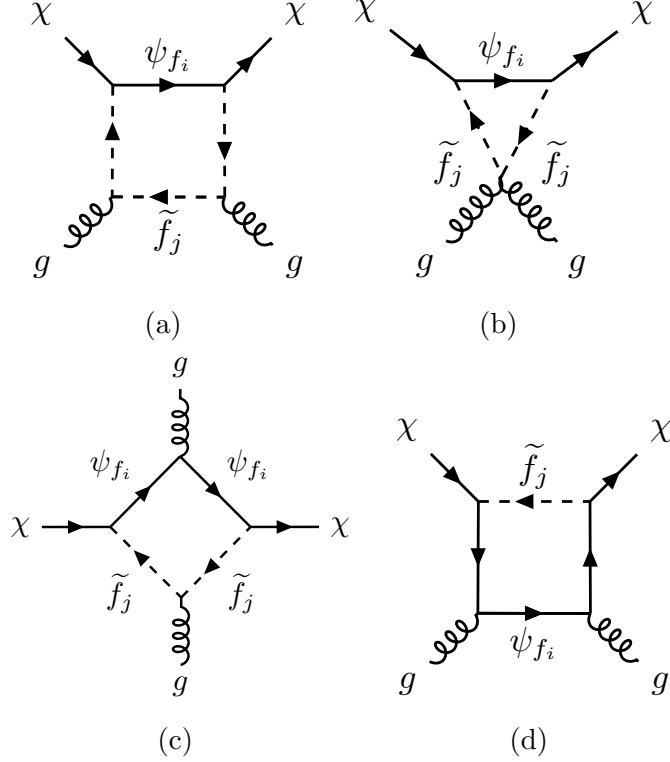


Figure 4: Feynman diagrams for effective DM-gluon interactions.

These quark/gluon operators then induce the spin-independent DM-nucleon interactions, which are described by

$$\mathcal{L}_{\text{eff-}N} = f_V^{(N)} \bar{\chi} \gamma^\mu \chi \bar{N} \gamma_\mu N + f_S^{(N)} \bar{\chi} \chi \bar{N} N , \quad (26)$$

where $N = p, n$ represents the nucleon field. The DM-nucleon vector coupling $f_V^{(N)}$ is readily obtained from the DM-quark couplings C_V^q as

$$f_V^{(p)} = 2C_V^{ru} + C_V^d , \quad f_V^{(n)} = C_V^{ru} + 2C_V^d . \quad (27)$$

On the other hand, to obtain the DM-nucleon scalar coupling $f_S^{(N)}$ from the quark/gluon scalar couplings C_S^q and C_S^g , we need the nucleon matrix elements of the quark scalar operators defined by $f_{T_q}^{(N)} \equiv \langle N | m_q \bar{q} q | N \rangle / m_N$ with m_N the nucleon mass. A recent compilation [36] gives

$$\begin{aligned} f_{T_u}^{(p)} &= 0.018(5) , & f_{T_d}^{(p)} &= 0.027(7) , & f_{T_s}^{(p)} &= 0.037(17) , \\ f_{T_u}^{(n)} &= 0.013(3) , & f_{T_d}^{(n)} &= 0.040(10) , & f_{T_s}^{(n)} &= 0.037(17) . \end{aligned} \quad (28)$$

At leading order in α_s , we then have [37]

$$\frac{f_S^{(N)}}{m_N} = \sum_{q=u,d,s} C_S^q f_{T_q}^{(N)} - \frac{8}{9} C_S^g f_{T_G}^{(N)} , \quad (29)$$

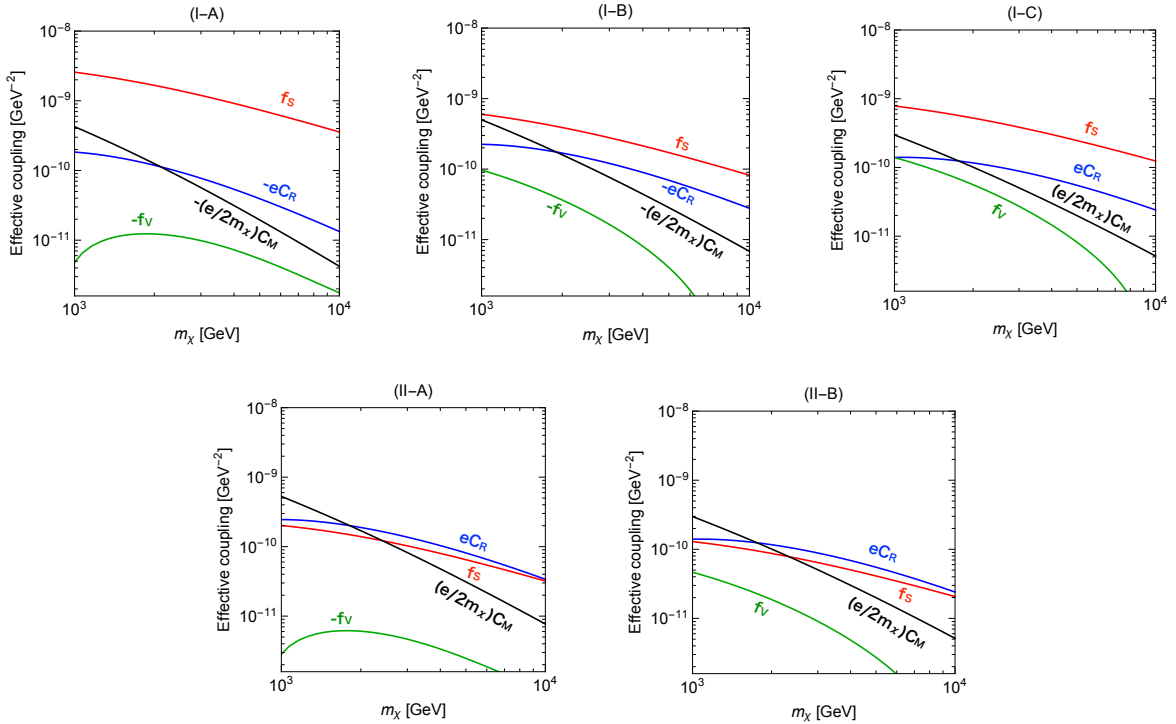


Figure 5: Green, red, blue, and black lines show the absolute values of $f_V^{(p)}$, $f_S^{(p)}$, eC_R^γ , and $eC_M^\gamma/(2m_\chi)$ as functions of the DM mass, respectively, with the minus sign indicated if the corresponding quantity is negative. Here we take the same parameter sets as in Fig. 2.

with $f_{TG}^{(N)} \equiv 1 - \sum_{q=u,d,s} f_{Tq}^{(N)}$.

To see the significance of the contributions of the vector and scalar interactions as well as that of the charge radius, in Fig. 5, we plot the absolute values of $f_V^{(p)}$, $f_S^{(p)}$, eC_R^γ , and $eC_M^\gamma/(2m_\chi)$ as functions of m_χ in the green, red, blue, and black lines, respectively, with the minus sign indicated if the corresponding quantity is negative. As we see below (Eq. (30)), these terms interfere with each other to give a contribution to the spin-independent charge-charge scattering of the DM with protons. We will see below that there is cancellation among these contributions. We also note that although $f_V^{(N)}$ and $f_S^{(N)}$ are induced by the dimension-less effective DM- Z and DM-Higgs couplings, they are suppressed as the DM mass gets large. This is because the generation of these couplings requires the electroweak-symmetry-breaking effect as mentioned in Appendix B, which results in an additional suppression factor with the heavy mass scale. From the dimensional analysis, $f_S^{(N)}$ is proportional to $1/m_\chi$ for $m_\chi \gg m_Z$ (m_Z : Z boson mass), while eC_R^γ , $eC_M^\gamma/2m_\chi$, and $f_V^{(N)}$ are scaled as $1/m_\chi^2$. In Fig. 5, eC_R^γ looks proportional to $1/m_\chi$ though we found it accidental.

4.2 Scattering cross section

By using the effective couplings obtained above, we evaluate the differential scattering cross section of the DM with a target nucleus with respect to the recoil energy E_R :

$$\begin{aligned} \frac{d\sigma_{\chi T}}{dE_R} = F_c^2(E_R) & \left[\frac{Z^2 e^2}{4\pi} \left(\frac{1}{E_R} - \frac{1}{E_R^{\max}(v_{\text{rel}}^2)} \right) (C_M^\gamma)^2 + \frac{Z^2 e^2}{4\pi v_{\text{rel}}^2} \frac{1}{E_R} (C_E^\gamma)^2 \right. \\ & \left. + \frac{m_T}{2\pi v_{\text{rel}}^2} \left| Z \left(f_S^{(p)} + f_V^{(p)} - eC_R^\gamma - \frac{e}{2m_\chi} C_M^\gamma \right) + (A - Z) \left(f_S^{(n)} + f_V^{(n)} \right) \right|^2 \right], \quad (30) \end{aligned}$$

where A , Z , and m_T are the atomic number, mass number, and mass of the target nucleus, respectively. \mathbf{v}_{rel} is the relative velocity of the DM and the target nucleus with $v_{\text{rel}} \equiv |\mathbf{v}_{\text{rel}}|$, and $E_R^{\max}(v_{\text{rel}}^2) = 2m_\chi^2 m_T v_{\text{rel}}^2 / (m_\chi + m_T)^2$ is the maximum recoil energy for a given v_{rel} . $F_c(E_R)$ is the nuclear form factor, for which we exploit the Lewin-Smith parametrization [38] of the Helm form factor [39]:

$$F_c^2(E_R) = \left(\frac{3j_1(qR)}{qR} \right)^2 e^{-q^2 s^2}, \quad (31)$$

with $j_1(x)$ a spherical Bessel function of the first kind, $q = \sqrt{2m_T E_R}$, $s = 0.9$ fm, $R = \sqrt{c^2 + \frac{7}{3}\pi^2 a^2 - 5s^2}$, $a = 0.52$ fm, and $c = (1.23A^{1/3} - 0.60)$ fm.

Figure 6 shows the first, second, and third terms in the square bracket in Eq. (30) as functions of the DM mass in the black, purple, and green lines, respectively; we refer to them as the MDM, EDM, and Contact contributions, respectively. Here we take the same parameter sets as in Fig. 2, with the solid (dashed) lines correspond to $\arg(b) = 0.1$ (1) degrees, and fix the rest of the parameters in Eq. (30) to be $E_R = 30$ keV, $v_{\text{rel}} = 232$ km/s, $Z = 54$, $A = 131$, and $m_T \simeq 122$ GeV (for ^{131}Xe). As we see, the Contact contributions in Model I-C, II-A, and II-B are much smaller than the MDM and EDM contributions due to the cancellation found in Fig. 5. Moreover, if there is a sizable CP violation in the DM couplings, the EDM contribution dominates the other contributions, since this contribution is strongly enhanced at low recoil energy because of the long-range photon exchange, as can be seen in Eq. (30).

4.3 Event rate

We are now ready to estimate the expected number of events in direct detection experiments. The differential event rate of the DM-target nuclei scattering process per unit detector mass is

$$\frac{dR}{dE_R} = \frac{\rho_{\text{DM}}}{m_T m_\chi} \int_{v_{\min}(E_R)}^{\infty} d^3 \mathbf{v}_{\text{rel}} v_{\text{rel}} f_{\oplus}(\mathbf{v}_{\text{rel}}) \frac{d\sigma_{\chi T}}{dE_R}, \quad (32)$$

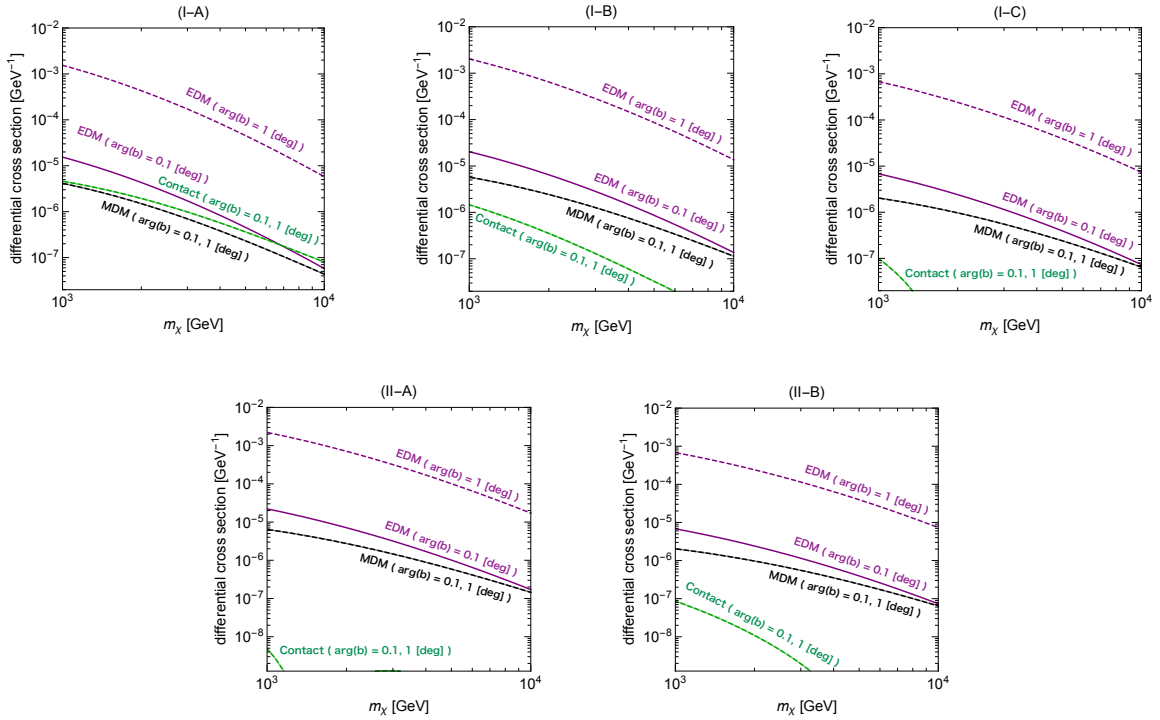


Figure 6: The first, second, and third terms in the square bracket in Eq. (30) as functions of DM mass in black, purple, and green lines, respectively. Here we take the same parameter sets as in Fig. 2, with the solid (dashed) lines correspond to $\arg(b) = 0.1$ (1) degrees, and fix the rest of the parameters in Eq. (30) to be $E_R = 30$ keV, $v_{\text{rel}} = 232$ km/s, $Z = 54$, $A = 131$, and $m_T \simeq 122$ GeV (for ^{131}Xe).

where ρ_{DM} is the local DM density, $f_{\oplus}(\mathbf{v}_{\text{rel}})$ is the DM velocity distribution in the lab frame, and $v_{\text{min}}(E_R)$ is the minimum speed required to yield recoil energy E_R :

$$v_{\text{min}}(E_R) = \sqrt{\frac{(m_{\chi} + m_T)^2 E_R}{2m_{\chi}^2 m_T}}. \quad (33)$$

For the DM velocity distribution, we assume a Maxwell-Boltzmann distribution in the galactic frame with a maximum speed that is set to be equal to the galaxy escape velocity v_{esc} ; namely,

$$f_{\oplus}(\mathbf{v}) = f(\mathbf{v} + \mathbf{v}_E), \quad (34)$$

with \mathbf{v}_E denotes the velocity of the Earth with respect to the galactic frame and

$$f(\mathbf{v}) = \begin{cases} \frac{1}{N} e^{-v^2/v_0^2} & (|\mathbf{v}| < v_{\text{esc}}) \\ 0 & (|\mathbf{v}| > v_{\text{esc}}) \end{cases}, \quad (35)$$

with

$$N = \pi^{3/2} v_0^3 \left[\operatorname{erf} \left(\frac{v_{\text{esc}}}{v_0} \right) - \frac{2v_{\text{esc}}}{\sqrt{\pi} v_0} e^{-\frac{v_{\text{esc}}^2}{v_0^2}} \right]. \quad (36)$$

From Eqs. (30) and (32), we see that to obtain the differential event rate we need to perform the following integrals with respect to the relative velocity:

$$\zeta(E_R) = \int_{v_{\min}(E_R)}^{\infty} \frac{d^3 \mathbf{v}_{\text{rel}}}{v_{\text{rel}}} f(\mathbf{v}_{\text{rel}} + \mathbf{v}_E), \quad \xi(E_R) = \int_{v_{\min}(E_R)}^{\infty} d^3 \mathbf{v}_{\text{rel}} v_{\text{rel}} f(\mathbf{v}_{\text{rel}} + \mathbf{v}_E). \quad (37)$$

We give analytical expressions for these integrals in Appendix C.

4.4 Direct detection bound

When we consider limits from direct detection experiments on a given model, it is often the case that we compute the DM-nucleon scattering cross section in the model and compare this with the bounds on this quantity obtained by direct detection experiments. In the present case, however, we are unable to adopt this strategy due to the following reasons. First, as can be seen in Eq. (30), the differential scattering cross section in our models may have several components that have different dependence on recoil energy, while in obtaining the direct detection limits the recoil-energy dependence is assumed to be the same as that of contact interactions (the second line in Eq. (30)). Second, the DM-proton scattering cross section may be quite different from that of the DM-neutron scattering in our model, while in the ordinary cases those two quantities are almost the same. Consequently, to study the current limits on our models from direct DM searches and their future prospects, we need to compute the number of events N_{event} in each direct detection experiment by integrating out dR/dE_R over the recoil energy E_R with taking account of the detection efficiency, and compare this with the results from the existing experiments or with the sensitivities expected in the future experiments.

The prescriptions for this procedure exploited in this paper are given for each direct detection experiment in Appendix D. In this work, we use the latest result from the XENON1T experiment [40] to obtain the current bound. For the estimate of future prospects, we consider the expected sensitivity of the XENONnT [41].⁸ To obtain the expected number of events, we use $\rho_{\text{DM}} = 0.3 \text{ GeV} \cdot \text{cm}^{-3}$, $v_0 = 220 \text{ km/s}$, $v_{\text{esc}} = 544 \text{ km/s}$, and $v_E = 232 \text{ km/s}$ as in Ref. [40].

In Fig. 7, we show the current constraints on the DM-MDM and DM-EDM as functions of the DM mass by the green shaded regions, which correspond to the XENON1T 90% C.L. exclusion limit [40]. Here, we adopt the normalization in Eq. (24), and assume $f_S^{(p)} = f_S^{(n)} = f_V^{(p)} = f_V^{(n)} = C_R^\gamma = 0$. We also show the sensitivity of XENONnT [41] in the green solid line. In addition, for comparison, we show the values of g_M and g_E predicted in Model I-A, which have already been shown in Fig. 2. It is found that the DM direct detection experiments are able to probe the singlet Dirac fermion DM at the TeV

⁸We have checked that the expected sensitivity of the LUX-ZEPLIN (LZ) [42] is quite similar to that of the XENONnT.

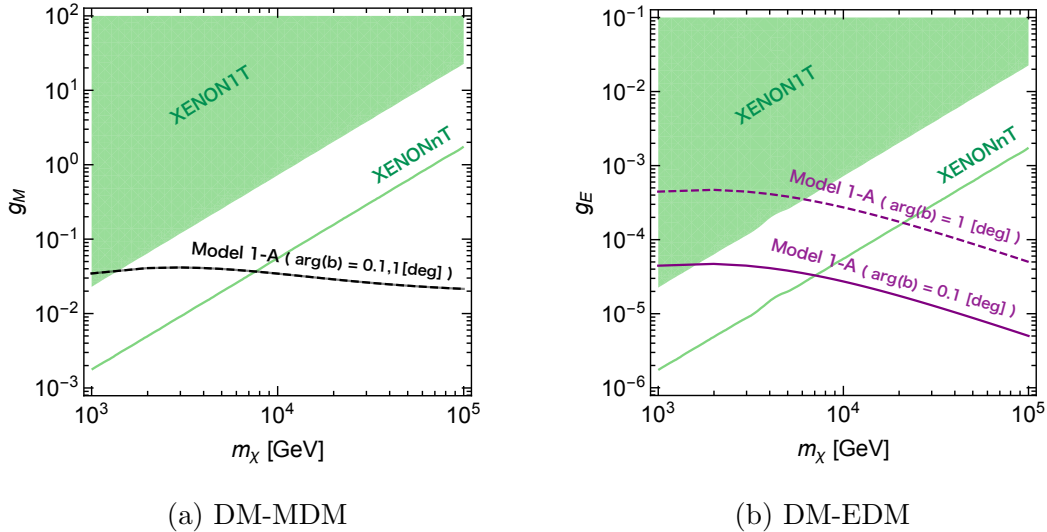


Figure 7: Current constraints from XENON1T [40] on the DM-MDM and DM-EDM as functions of the DM mass shown in the green shaded regions, as well as the sensitivity of XENONnT [41] in the green solid line. We also show values of g_M and g_E predicted in Model I-A, which have already been shown in Fig. 2.

scale through the MDM and EDM interactions; in particular, the EDM interaction may allow us to probe the DM with a mass of as large as $\mathcal{O}(10)$ TeV if there is a sizable CP violation in the DM couplings. More detailed analysis for each model is given in Sec. 6.

5 Electric Dipole Moments

As we mentioned above, the DM-EDM is induced only in the presence of CP phases in the couplings of new particles. Such CP phases may also induce CP-odd quantities in the SM sector, which can be probed via the measurements of the EDMs of electron and nucleons. In this section, we evaluate these EDMs induced in our models.

5.1 CP violation in the DM interactions

Let us first consider the case with $\varphi_{\mu_f} \neq 0$. In this case, in Model I, the non-zero CP phase φ_{μ_f} induces the Weinberg operator [12] at the two-loop level through the diagram depicted in Fig. 8:⁹

$$\mathcal{L}_{\mathcal{O}\mathcal{P}} = -\frac{1}{6}w f^{ABC} \epsilon^{\mu\nu\rho\sigma} G_{\mu\lambda}^A G_{\nu}^{B\lambda} G_{\rho\sigma}^C, \quad (38)$$

⁹ $\varphi_{A\bar{f}}$ also induces the Weinberg operator, but this contribution is smaller than that from φ_{μ_f} as it is always accompanied by the insertion of Higgs VEVs.

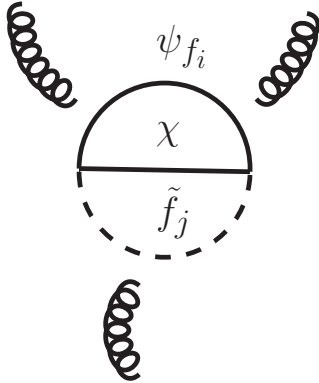


Figure 8: Feynman diagram that induces the Weinberg operator. The gluon lines are attached to the vector-like quark and/or scalar lines.

where f^{ABC} denotes the structure constants of $SU(3)$ and $\epsilon^{\mu\nu\rho\sigma}$ is the totally antisymmetric tensor with $\epsilon^{0123} = 1$. We give an analytical expression for the Wilson coefficient w in Appendix E.1, which we derive from generic results obtained in Ref. [43].

This Weinberg operator induces non-zero EDMs of nucleons, which are estimated by means of the QCD sum rules [44]:

$$d_N(w)/e = \pm(10 - 30) \text{ MeV} \times w(1 \text{ GeV}) , \quad (39)$$

for $N = n, p$, where $w(1 \text{ GeV})$ denotes the Wilson coefficient of the Weinberg operator at the scale of 1 GeV. In our numerical analysis, we use $d_N(w)/e = +20 \text{ MeV} \times w(1 \text{ GeV})$ as a reference value. We obtain $w(1 \text{ GeV})$ by evolving the Wilson coefficient from the matching scale down to 1 GeV according to the renormalization group equation (RGE). The RGE for w at the leading order is given by [45]

$$\frac{d}{d \ln \mu_R} w(\mu_R) = \frac{\alpha_s(\mu_R)}{4\pi} (N_c + 2N_f) w(\mu_R) , \quad (40)$$

where $N_c = 3$ and N_f are the numbers of colors and quark flavors, respectively, and μ_R denotes the renormalization scale.

In Fig. 9, we show the nucleon EDM induced by the CP-violating couplings between the DM and the mediator fields. Here, we take the same parameter sets as in Model I-A in Fig. 2, with $\arg(b) = 0.1$ and 45 degrees in the black solid and dashed lines, respectively. The dark and light magenta regions correspond to the current bound on the neutron EDM ($|d_n| \geq 2.9 \times 10^{-26} e \cdot \text{cm}$ [46]) and the future prospects for the observation of the proton EDM ($|d_p| \geq 2.5 \times 10^{-29} e \cdot \text{cm}$ [47]), respectively. As we see, although the present limit is not sensitive to the CP phases in the DM couplings yet, they may be probed in future measurements of the nucleon EDMs. Notice that the Weinberg operator depends on the CP phases in the DM couplings in the same manner as the DM EDM, as we see from Eqs. (50) and (110). We thus expect a strong correlation between the DM-nucleus

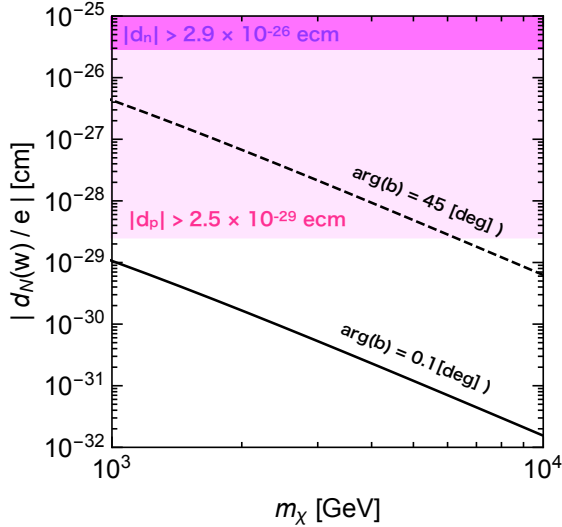


Figure 9: Nucleon EDM induced by the CP-violating interactions between the DM and the mediator fields. We take the same parameter sets as in Model I-A in Fig. 2, with $\arg(b) = 0.1$ and 45 degrees in black solid and dashed lines, respectively. Dark and light magenta regions correspond to the current bound on the neutron EDM ($|d_n| \geq 2.9 \times 10^{-26} e \cdot \text{cm}$ [46]) and the future prospects for the observation of the proton EDM ($|d_p| \geq 2.5 \times 10^{-29} e \cdot \text{cm}$ [47]), respectively.

scattering cross section and the nucleon EDM with respect to the CP phases in the DM couplings, which we actually see in the subsequent section.

5.2 CP violation in the vector-like fermion-Higgs couplings

The CP phases in the vector-like fermion-Higgs couplings, $\varphi_{\kappa_{\bar{f}}}$, can also be probed in EDM experiments, as they induce the electron EDM at two-loop level through the Barr-Zee diagrams [51] shown in Fig. 10:

$$\mathcal{L}_e = -\frac{i}{2} d_e \bar{e} \sigma^{\mu\nu} \gamma_5 e F^{\mu\nu} . \quad (41)$$

The resultant expressions for these two-loop contributions are summarized in Appendix E.2. The predicted values of the electron EDM in Model I and II are then given in Figs. 11 and 12. In Fig. 11, we show each contribution to the electron EDM as a function of the fermion mass parameter μ . The black, red, blue, and green lines represent the total, WW , $h\gamma$, and hZ contributions, respectively, with the sign of each contribution indicated explicitly. Here, the $h\gamma$ and hZ contributions come from the upper left diagram while the WW contribution from the other diagrams in Fig. 10. We set $\mu_Q = \mu_L = \mu + 100$ GeV, $\mu_{\bar{u}} = \mu + 50$ GeV, $\mu_{\bar{d}} = \mu_{\bar{e}} = \mu$, $\kappa = \kappa_{\bar{f}} = \kappa'_{\bar{f}}$, $|\kappa| = 0.5$, and $\arg(\kappa) = 45$ deg.

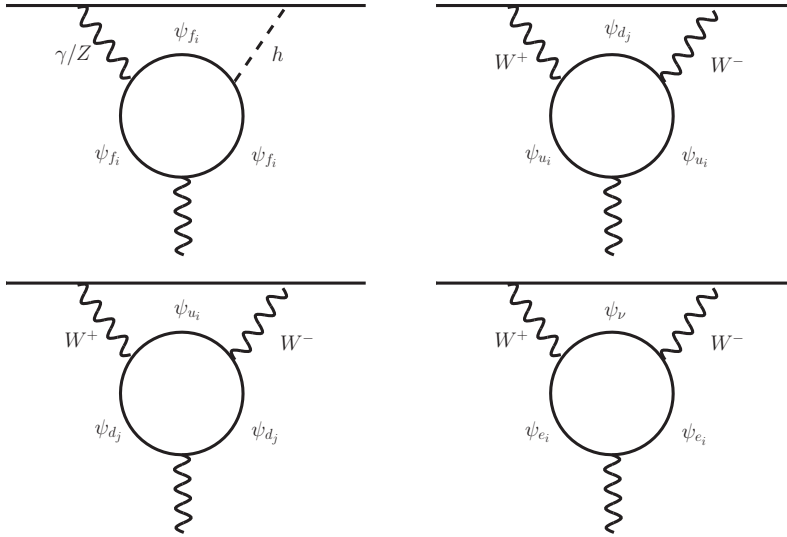


Figure 10: Barr-Zee diagrams for electron EDM.

The dark and light gray areas correspond to the present bound on the electron EDM ($|d_e| \geq 8.7 \times 10^{-29} e \cdot \text{cm}$ [48]) and the future prospects for the observation of the electron EDM ($|d_e| \geq 1.0 \times 10^{-30} e \cdot \text{cm}$ [49, 50]), respectively. As we see, the signs of the WW contributions in Model I and II are different from each other. We then show the contour plots for the electron EDM in the μ - $\arg(\kappa)$ plane in Fig. 12, with the same parameter sets except for $\arg(\kappa)$. These plots show that even the present limit gives a strong constraint on the vector-like fermions at the TeV scale if there is an $\mathcal{O}(1)$ CP phase in their couplings, which may be pushed down to as strong as $\mathcal{O}(0.01)$ in the future.

In Model I, a non-zero value of $\varphi_{\kappa_{\bar{f}}}$ also induces the EDM and chromo-EDM of quarks through the Barr-Zee diagrams,¹⁰ which then give rise to the nucleon EDMs. We see however that the limit from the neutron EDM is weaker than that from the electron EDM; we hence do not give further analyses on this here, though we provide an analytical expression of the quark chromo-EDM in Appendix E.2 just for completeness. Nevertheless, we note in passing that the quark EDM and chromo-EDM can be important when we discuss the effect of the Weinberg operator considered in the previous subsection, as all of these quantities can give comparable contributions to nucleon EDM.

6 Results

Now we study the experimental constraints discussed above on the parameter space of our models and assess their testability. We again consider the simplified scenarios described in Sec. 4 with parameters taken to be $a = |b| = 1$, $\lambda'_Q = \lambda'_L = 0$, $\lambda_f = \kappa_{\bar{f}} = \kappa'_{\bar{f}} = 0.5$,

¹⁰For the contribution to the quark chromo-EDM, the relevant diagram is obtained from the upper left diagram in Fig. 10 by replacing the γ/Z lines with gluon lines.

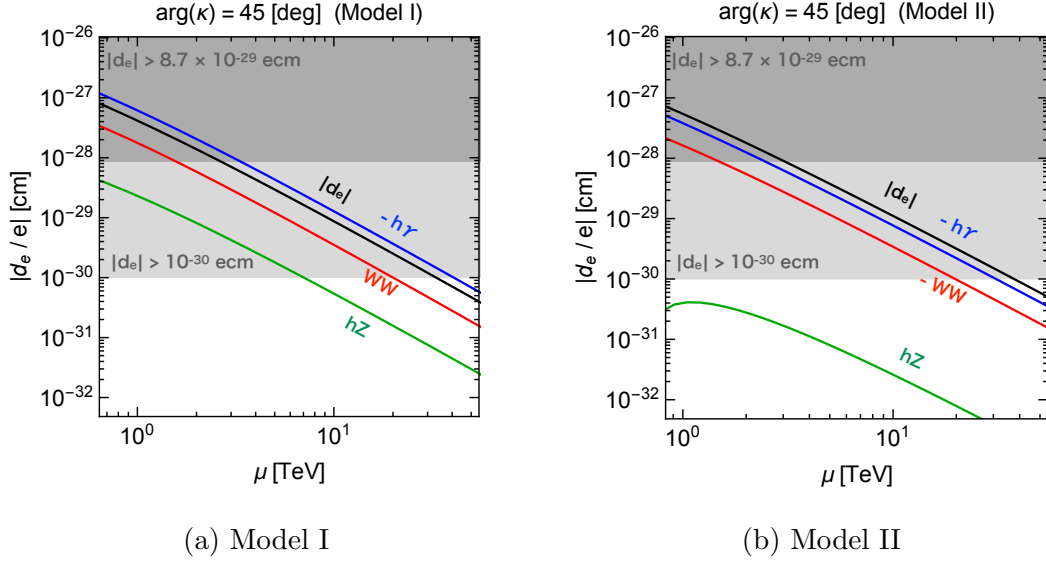


Figure 11: Each contribution to the electron EDM as a function of the fermion mass parameter μ . Black, red, blue, and green lines show the total, WW , $h\gamma$, and hZ contributions, respectively, with the sign of each contribution indicated explicitly. We set $\mu_Q = \mu_L = \mu + 100$ GeV, $\mu_{\bar{u}} = \mu + 50$ GeV, $\mu_{\bar{d}} = \mu_{\bar{e}} = \mu$, $\kappa = \kappa_{\bar{f}} = \kappa'_{\bar{f}}$, $|\kappa| = 0.5$, and $\arg(\kappa) = 45$ deg. Dark and light gray areas correspond to the present bound on the electron EDM ($|d_e| \geq 8.7 \times 10^{-29} e \cdot \text{cm}$ [48]) and the future prospects for the observation of the electron EDM ($|d_e| \geq 1.0 \times 10^{-30} e \cdot \text{cm}$ [49, 50]), respectively.

$\mu_Q = \mu_L = 800$ GeV, $\mu_{\bar{u}} = 750$ GeV, $\mu_{\bar{d}} = \mu_{\bar{e}} = 700$ GeV, $\tilde{m}_Q = \tilde{m}_L = 1.2M$, $\tilde{m}_{\bar{u}} = 1.1M$, $\tilde{m}_{\bar{d}} = \tilde{m}_{\bar{e}} = M$, $A_{\bar{f}} = 2M$, and $M = 1.1m_\chi$.

Let us begin with the CP-conserving cases. Figure 13 shows the current limits provided by XENON1T [40] (green shaded area) and the expected sensitivity of XENONnT [41] (green solid line) in the parameter space of each model. The gray shaded area represents the region where the DM density exceeds the observed value: $\Omega_{\text{DM}} h^2 \geq 0.12$. Here, we take $\arg(b) = 0$. We find that at present the allowed region with $\Omega_{\text{DM}} h^2 \leq 0.12$ exists in all of the models, where the masses of both the DM and new scalar particles are predicted to be at the TeV scale. All of these allowed regions can be fully probed in the future direct detection experiments.

Next we discuss the cases where there is a non-zero CP phase in the DM-mediator interactions. In Fig. 14, we again show current limits provided by XENON1T [40] (green shaded area) and the expected sensitivity of XENONnT [41] (green solid line) in the parameter space of each model, where we now vary $\arg(b)$. We also show the predicted values of the nucleon EDM in the magenta solid lines, as well as the expected reach provided by the future nucleon EDM search, $|d_p| \geq 2.5 \times 10^{-29} e \cdot \text{cm}$ [47], in the magenta shaded region. The gray shaded area represents the region where the DM density exceeds the observed value: $\Omega_{\text{DM}} h^2 \geq 0.12$. Here we take $m_\chi = 3$ TeV, 2 TeV, 2 TeV, 2 TeV,

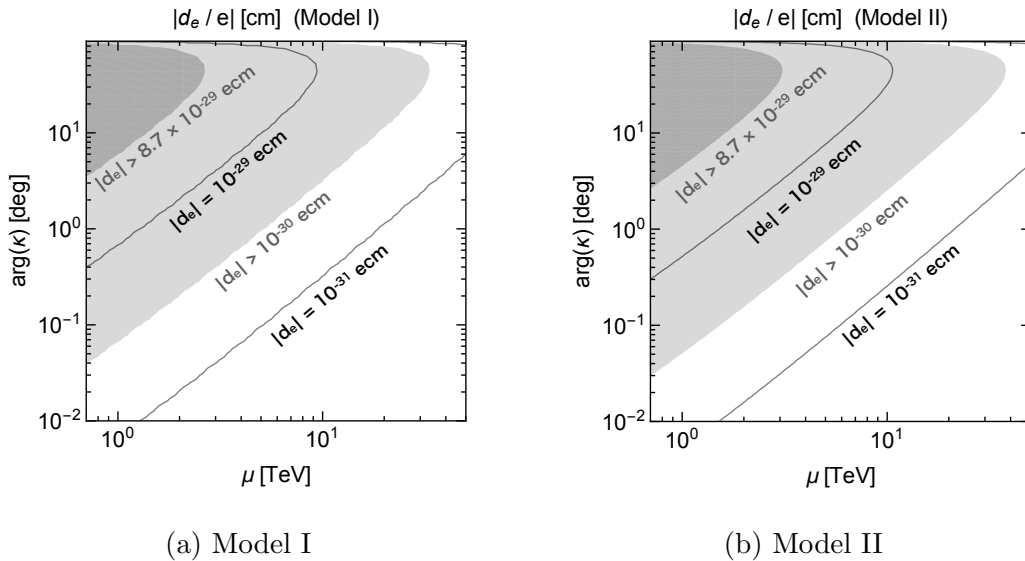


Figure 12: Contour plots for the electron EDM. We take the same parameters as in Fig. 11 except for $\arg(\kappa)$. Dark and light gray areas correspond to the present bound on the electron EDM ($|d_e| \geq 8.7 \times 10^{-29} e \cdot \text{cm}$ [48]) and the future prospects for the observation of the electron EDM ($|d_e| \geq 1.0 \times 10^{-30} e \cdot \text{cm}$ [49, 50]), respectively.

and 1.5 TeV in the cases of Model I-A, I-B, I-C, II-A, and II-B, respectively. We see that the limits from the direct detection experiments get quite strong in the presence of the CP phases in the DM-mediator interactions due to the large contribution of the DM EDM. Indeed, if the CP phases are $\mathcal{O}(1)$, the current limits are so severe that most of the parameter space with $\Omega_{\text{DM}} h^2 \leq 0.12$ has already been disfavored. In addition, we see a correlation between the direct detection bound and the predicted value of the nucleon EDM in the case of Model I, as expected, though it turns out that the regions which can be covered by the future nucleon EDM searches have already been excluded by the XENON1T limit. We however note that EDM experiments may still be able to probe both Model I and II since CP phases in the vector-like-fermion-Higgs couplings induce the electron and nucleon EDMs without generating the DM EDM, as we see in the previous section. All in all, even though the relevant physical observables (such as the DM detection rate and electron/nucleon EDMs) are always induced at loop level in the singlet Dirac fermion DM scenarios discussed in this paper, they are still detectable in the forthcoming experiments, and thus these scenarios could be put on the table to be thoroughly investigated in the future.

7 Conclusion

In this paper, we have studied simplified models for a singlet Dirac fermion DM which interacts with the SM particles only through radiative corrections. We have considered

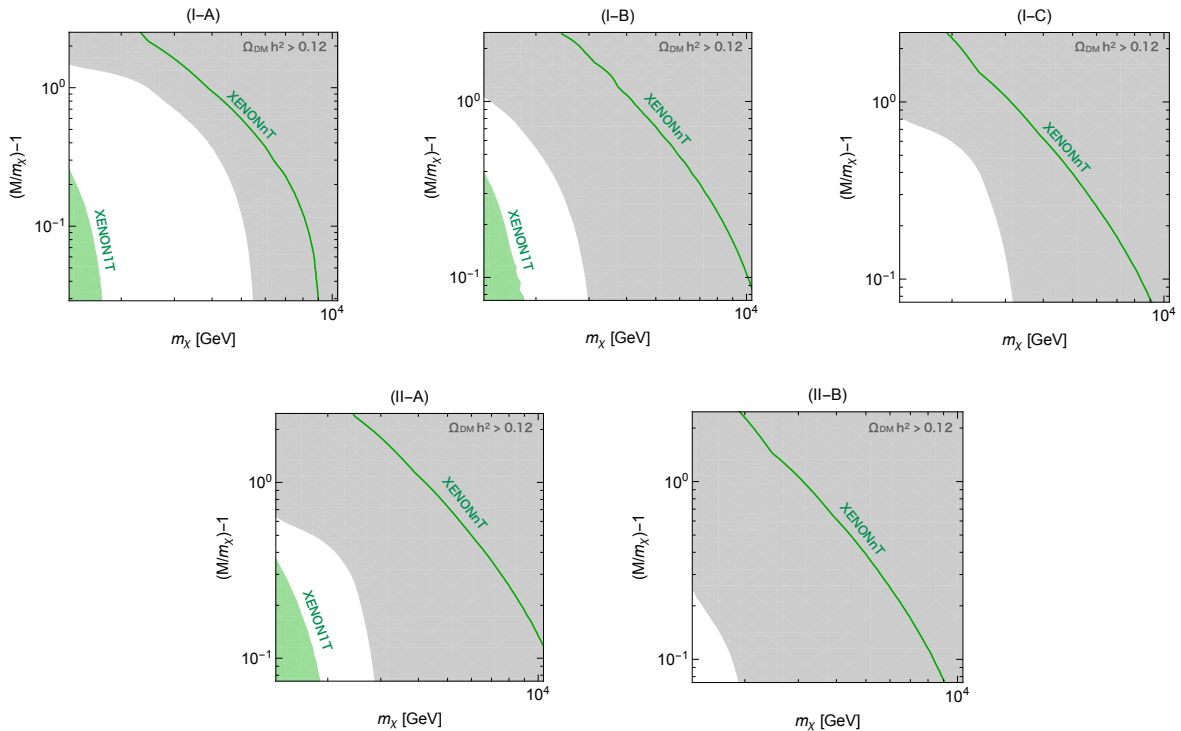


Figure 13: Current limits provided by XENON1T [40] (green shaded area) and expected sensitivity of XENONnT [41] (green solid line) in the parameter space of each model. The gray shaded area represents the region where the DM density exceeds the observed value: $\Omega_{\text{DM}} h^2 \geq 0.12$. Here, we take $\arg(b) = 0$.

the cases where certain sets of vector-like fermions and complex scalars are introduced as mediator fields, which are supposed to interact with the SM gauge and Higgs bosons at the renormalizable level. The Dirac fermion DM has phenomenologically distinct features as it is able to have vector and tensor couplings, which in general result in a large DM-nucleus scattering rate. In addition, the Dirac fermion DM particles can pair-annihilate in the s -wave processes without suffering from a chirality suppression, which allows the DM to avoid overproduction even if the DM mass is > 1 TeV. Indeed, we have found that the right amount of DM abundance is obtained for a DM mass of $\mathcal{O}(1)$ TeV with $\mathcal{O}(1)$ DM-mediator couplings, if vector-like fermions are lighter than the Dirac fermion DM.

These simplified models generically introduce new CP phases in the couplings. If there is a CP phase in the DM-mediator couplings, the DM acquires an EDM, which strongly enhances the DM-nucleus scattering cross section. Such a CP phase also induces nucleon EDMs via the Weinberg operator if the mediator fields have color charges (Model I). Even if the mediators are non-colored particles, CP phases in the couplings between the vector-like fermions and the SM Higgs field generate the electron and nucleon EDMs through the Barr-Zee diagrams.

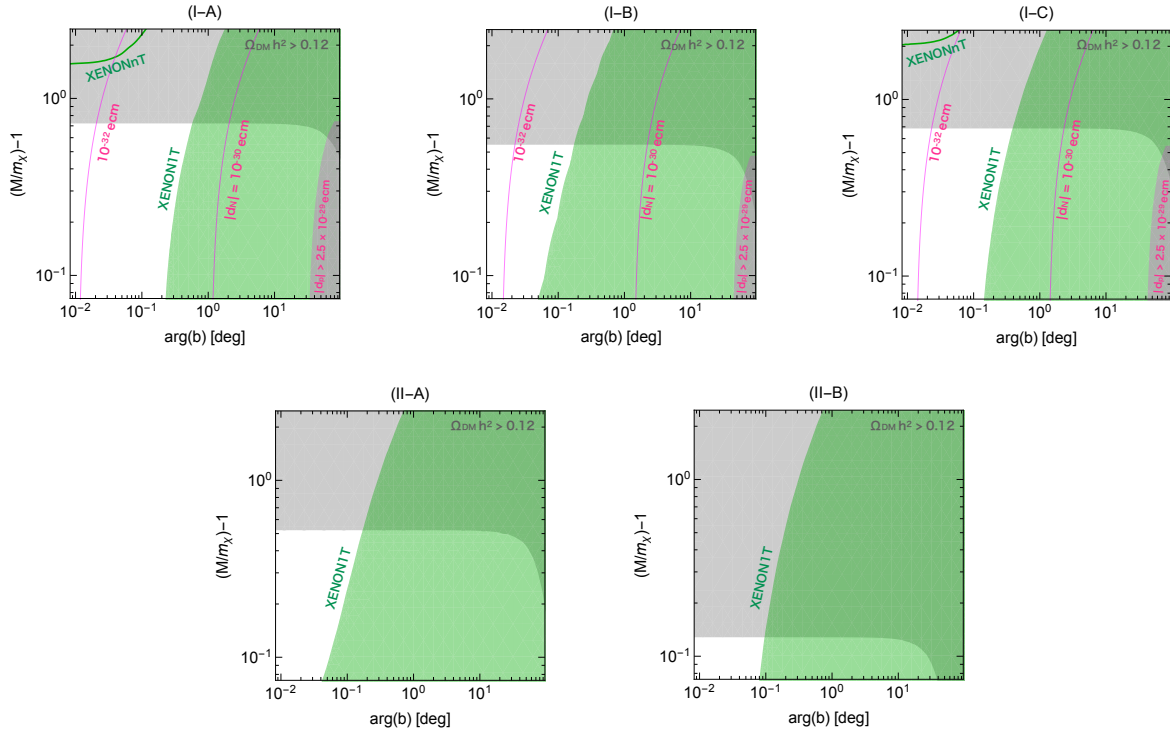


Figure 14: Current limits provided by XENON1T [40] (green shaded area) and expected sensitivity of XENONnT [41] (green solid line) in the parameter space of each model. We also show the predicted values of the nucleon EDM in the magenta solid lines, as well as the expected reach provided by the future nucleon EDM search, $|d_p| \geq 2.5 \times 10^{-29} e \cdot \text{cm}$ [47], in the magenta shaded region. The gray shaded area represents the region where the DM density exceeds the observed value: $\Omega_{\text{DM}} h^2 \geq 0.12$. Here we take $m_\chi = 3 \text{ TeV}$, 2 TeV , 2 TeV , 2 TeV , and 1.5 TeV in the cases of Model I-A, I-B, I-C, II-A, and II-B, respectively.

To see the experimental implications of the rich phenomenology of the Dirac fermion DM, in this paper, we consider the DM direct detection experiments and the EDM measurements, with particular emphasis on the effect of CP phases on the observables in these experiments. For direct detection experiments, it turns out that the current limit set by the XENON1T experiment has already started to be excluded the parameter space. In particular, if there is a sizable CP phase in the DM-mediator couplings, the DM direct detection rate is significantly enhanced due to the DM-EDM contribution via the photon exchange so that even the current limit excludes a wide range of the parameter space. We also find that the future DM experiments can basically probe all of the parameter region favored by the thermal relic abundance of the DM. As mentioned above, CP phases in the DM-mediator couplings, which generate the DM-EDM, also induce the nucleon EDMs in Model I, and in fact we have found a correlation between these observables.

It is found that the future measurements of nucleon EDMs are less promising compared with the DM direct detection experiments if these phases are the only source of the extra CP violation. If, on the other hand, there are CP phases in the couplings between the vector-like fermions and the SM Higgs field, these phases induce the electron EDM, which may be probed in the future experiments if the vector-like fermions are at $\mathcal{O}(1)$ TeV. Consequently, even though the relevant observables are generated only at the loop level, both the DM direct searches and the EDM experiments are quite promising for testing the singlet Dirac DM scenario discussed in this paper, which makes this scenario a suitable benchmark for the forthcoming experiments.

Acknowledgments

This work is supported in part by the Grant-in-Aid for Innovative Areas (16H06492 [JH], 16H06490 [RN], 18H05542 [NN]) and Young Scientists B (17K14270 [NN]). The work of JH is also supported by World Premier International Research Center Initiative (WPI Initiative), MEXT, Japan. NN would like to thank E-ken at Nagoya University for hospitality while this work was initiated.

Appendix

A Interactions in Mass Eigenbasis

In this section, we write down the interactions of the new particles in the mass eigenbasis. We here use the four-component notation, with vector-like fermion mass eigenstates defined by

$$\psi_{f_i} \equiv \begin{pmatrix} \psi_{f_i L} \\ \psi_{f_i R} \end{pmatrix}. \quad (42)$$

A.1 Gauge interactions

We list the gauge interaction terms that are relevant for the discussion in this paper.

$$\begin{aligned} \mathcal{L}_{\text{gauge}} = & -eA_\mu \sum_{f,i} Q_f \bar{\psi}_{f_i} \gamma^\mu \psi_{f_i} - g_Z Z_\mu \sum_{f,i,j} \bar{\psi}_{f_i} \gamma^\mu (C_{fZL}^{ij} P_L + C_{fZR}^{ij} P_R) \psi_{f_j} \\ & - \frac{g}{\sqrt{2}} \left[\bar{\psi}_{u_i} \gamma^\mu W_\mu^+ (C_{QWL}^{ij} P_L + C_{QWR}^{ij} P_R) \psi_{d_j} + \bar{\psi}_\nu \gamma^\mu W_\mu^+ (C_{LWL}^i P_L + C_{LWR}^i P_R) \psi_{e_i} + \text{h.c.} \right] \\ & - ieA_\mu \sum_{f,i} Q_f \tilde{f}_i^* \overleftrightarrow{\partial}^\mu \tilde{f}_i - ig_Z Z_\mu \sum_{f,i,j} \tilde{C}_{fZ}^{ij} \tilde{f}_i^* \overleftrightarrow{\partial}^\mu \tilde{f}_j + \dots, \end{aligned} \quad (43)$$

with

$$\begin{aligned} C_{fZL/R}^{ij} &= (V_{fL/R})_{1i}^* (V_{fL/R})_{1j} T_{3f} - Q_f \sin^2 \theta_W \delta_{ij}, \\ C_{QWL/R}^i &= (V_{uL/R})_{1i}^* (V_{dL/R})_{1j}, \quad C_{LWL/R}^i = e^{\pm \frac{i}{2} \theta_L} (V_{eL/R})_{1i}, \\ \tilde{C}_{fZ}^{ij} &= (\tilde{V}_f)_{1i}^* (\tilde{V}_f)_{1j} T_{3f} - Q_f \sin^2 \theta_W \delta_{ij}, \end{aligned} \quad (44)$$

where $e > 0$ is the electric charge of positron, $g_Z \equiv \sqrt{g'^2 + g^2}$, g' and g are the gauge coupling constants of $U(1)_Y$ and $SU(2)_L$, respectively, $P_{L/R} \equiv (1 \mp \gamma_5)/2$, Q_f and T_{3f} are the electric charge and the weak isospin of the fermion f , respectively, θ_W is the weak mixing angle, and $A \overleftrightarrow{\partial}_\mu B \equiv A(\partial_\mu B) - (\partial_\mu A)B$.

A.2 Higgs couplings

The relevant part of the Higgs interactions is

$$\mathcal{L}_{\text{Higgs}} = -\frac{1}{\sqrt{2}} \sum_{f,i,j} h \bar{\psi}_{f_i} (C_{fhL}^{ij} P_L + C_{fhr}^{ij} P_R) \psi_{f_j} - \frac{1}{\sqrt{2}} \sum_{f,i,j} \tilde{C}_{fh}^{ij} h \tilde{f}_i^* \tilde{f}_j, \quad (45)$$

with

$$\begin{aligned}
C_{fhL}^{ij} &= \left[\kappa_{\bar{f}} (V_{fR})_{2i}^* (V_{fL})_{1j} + \kappa'_{\bar{f}} (V_{fR})_{1i}^* (V_{fL})_{2j} \right] , \\
C_{fhR}^{ij} &= (C_{fhL}^{ij})^* , \\
\tilde{C}_{fh}^{ij} &= \left[A_{\bar{f}} (\tilde{V}_f)_{2i}^* (\tilde{V}_f)_{1j} + A_{\bar{f}}^* (\tilde{V}_f)_{1i}^* (\tilde{V}_f)_{2j} \right] \\
&\quad + v \left[(\lambda_f - 2T_{3f} \lambda'_f) (\tilde{V}_f)_{1i}^* (\tilde{V}_f)_{1j} + \lambda_{\bar{f}} (\tilde{V}_f)_{2i}^* (\tilde{V}_f)_{2j} \right] ,
\end{aligned} \tag{46}$$

where $\lambda_u^{(\prime)} = \lambda_d^{(\prime)} \equiv \lambda_Q^{(\prime)}$, $\lambda_\nu^{(\prime)} = \lambda_e^{(\prime)} \equiv \lambda_L^{(\prime)}$, and $\lambda_{\bar{\nu}} = 0$.

A.3 Dark matter couplings

In the mass eigenbasis, the terms in Eq. (4) are given as follows:

$$\mathcal{L}_{\chi f \bar{f}} = \bar{\chi} (C_{f\chi L}^{ij} P_L + C_{f\chi R}^{ij} P_R) \psi_{f_i} \tilde{f}_j^* + \text{h.c.} , \tag{47}$$

with

$$\begin{aligned}
C_{f\chi L}^{ij} &= e^{-\frac{i}{2}\theta_\chi} \left[a_f (V_{fL})_{1i} (\tilde{V}_f)_{1j}^* + a_{\bar{f}} (V_{fL})_{2i} (\tilde{V}_f)_{2j}^* \right] , \\
C_{f\chi R}^{ij} &= e^{\frac{i}{2}\theta_\chi} \left[b_f^* (V_{fR})_{1i} (\tilde{V}_f)_{1j}^* + b_{\bar{f}}^* (V_{fR})_{2i} (\tilde{V}_f)_{2j}^* \right] ,
\end{aligned} \tag{48}$$

where $a_u = a_d \equiv a_Q$, $b_u = b_d \equiv b_Q$, $a_\nu = a_e \equiv a_L$, $b_\nu = b_e \equiv b_L$, and $a_{\bar{\nu}} = b_{\bar{\nu}} = 0$.

B Effective Interactions of Singlet Dirac Fermion DM

In this appendix, we summarize the one-loop formulae for the Wilson coefficients of the effective operators considered in Sec. 4.

B.1 DM-photon effective interactions

The Wilson coefficients of the DM-photon effective interactions given in Eq. (23), which are induced by the diagrams shown in Fig. 1, are computed as

$$C_M^\gamma = \frac{e}{(4\pi)^2 m_\chi} \sum_{f,i,j} N_c Q_f \left\{ C_{f\chi SS}^{ij} g_{M1}(m_\chi, \tilde{m}_{f_j}, m_{f_i}) + \frac{m_{f_i}}{m_\chi} \text{Re} [C_{f\chi L}^{ij} C_{f\chi R}^{ij*}] g_{M2}(m_\chi, \tilde{m}_{f_j}, m_{f_i}) \right\} , \tag{49}$$

$$C_E^\gamma = \frac{e}{(4\pi)^2 m_\chi^2} \sum_{f,i,j} N_c Q_f m_{f_i} \text{Im} [C_{f\chi L}^{ij} C_{f\chi R}^{ij*}] g_{E1}(m_\chi, \tilde{m}_{f_j}, m_{f_i}) , \tag{50}$$

$$C_R^\gamma = \frac{e}{(4\pi)^2 m_\chi^2} \sum_{f,i,j} N_c Q_f \left\{ C_{f\chi SS}^{ij} g_{R1}(m_\chi, \tilde{m}_{f_j}, m_{f_i}) + \frac{m_{f_i}}{m_\chi} \text{Re} [C_{f\chi L}^{ij} C_{f\chi R}^{ij*}] g_{R2}(m_\chi, \tilde{m}_{f_j}, m_{f_i}) \right\} , \tag{51}$$

where

$$C_{f\chi SS}^{ij} \equiv \frac{1}{2} \{ |C_{f\chi L}^{ij}|^2 + |C_{f\chi R}^{ij}|^2 \} , \quad (52)$$

and N_c is the color factor: $N_c = 3$ (1) for Model I (II). The mass functions in the above expressions are given by

$$g_{M1}(m_\chi, M, m) = 1 - \frac{M^2 - m^2}{2m_\chi^2} \ln\left(\frac{M^2}{m^2}\right) + \frac{\Delta + m_\chi^2(M^2 - m_\chi^2 + m^2)}{2m_\chi^2} L , \quad (53)$$

$$g_{M2}(m_\chi, M, m) = \frac{1}{2} \left[\ln\left(\frac{M^2}{m^2}\right) - (M^2 + m_\chi^2 - m^2)L \right] , \quad (54)$$

$$g_{E1}(m_\chi, M, m) = g_{M2}(m_\chi, M, m) , \quad (55)$$

$$g_{R1}(m_\chi, M, m) = \frac{1}{12} \left[\frac{8(M^2 - m^2) + m_\chi^2}{m_\chi^2} \ln\left(\frac{M^2}{m^2}\right) - \frac{4}{\Delta} \{ 4\Delta + m_\chi^2(M^2 + 3m^2) - m_\chi^4 \} \right. \\ \left. - \frac{1}{m_\chi^2 \Delta} \{ 8\Delta^2 + (9M^2 - 5m_\chi^2 + 7m^2)m_\chi^2 \Delta - 4m^2 m_\chi^4 (3M^2 - m_\chi^2 + m^2) \} L \right] , \quad (56)$$

$$g_{R2}(m_\chi, M, m) = \frac{1}{3} \left[-\ln\left(\frac{M^2}{m^2}\right) + \frac{2m_\chi^2(M^2 - m^2)}{\Delta} \right. \\ \left. + \frac{M^2 - m^2}{\Delta} \{ \Delta + m_\chi^4 - m_\chi^2(M^2 + m^2) \} L \right] , \quad (57)$$

where¹¹

$$\Delta(m_\chi^2, M^2, m^2) \equiv m_\chi^4 - 2m_\chi^2(M^2 + m^2) + (M^2 - m^2)^2 , \quad (58)$$

and

$$L(m_\chi^2, M^2, m^2) \equiv \begin{cases} \frac{1}{\sqrt{\Delta}} \ln\left(\frac{M^2 + m^2 - m_\chi^2 + \sqrt{\Delta}}{M^2 + m^2 - m_\chi^2 - \sqrt{\Delta}}\right) & (\Delta > 0) \\ \frac{2}{\sqrt{|\Delta|}} \arctan\left(\frac{\sqrt{|\Delta|}}{M^2 + m^2 - m_\chi^2}\right) & (\Delta < 0) \end{cases} . \quad (59)$$

We have checked that μ_χ and b_χ in Ref. [8] are reproduced from the above expressions for C_M^γ and C_R^γ , respectively, by taking $C_{f\chi L}^{ij} = 0$, and C_M^γ , C_E^γ , and C_R^γ are consistent with those given in Ref. [10]. From Eq. (50), we see that the DM-EDM can be generated only in the presence of the left-right mixing as well as a non-zero imaginary component of the product $C_{f\chi L}^{ij} C_{f\chi R}^{ij*}$, which are not required for the generation of DM-MDM and DM charge radius.

¹¹ Δ can be factorized as $\Delta = (M - m_\chi - m)(M - m_\chi + m)(M + m_\chi - m)(M + m_\chi + m)$.

B.2 DM- Z effective interactions

The diagrams in Fig. 1 also generate the effective DM- Z vector coupling,¹² which gives rise to the DM-quark vector interactions. In the broken phase, this coupling is represented by

$$\mathcal{L}_{\chi Z} = -g_Z C_{\chi Z} \bar{\chi} \gamma^\mu \chi Z_\mu, \quad (60)$$

where the coupling $C_{\chi Z}$ is given by

$$\begin{aligned} C_{\chi Z} = & \frac{1}{(4\pi)^2} \sum_{f,i,j,k} N_c [C_{fZ1}^{kij} g_{Z1}(m_\chi, \tilde{m}_{f_k}, m_{f_i}, m_{f_j}) \\ & + C_{fZ2}^{kij} g_{Z2}(m_\chi, \tilde{m}_{f_k}, m_{f_i}, m_{f_j}) + C_{fZ3}^{kij} g_{Z3}(m_\chi, \tilde{m}_{f_k}, m_{f_i}, m_{f_j}) \\ & + \tilde{C}_{fZ1}^{jki} \tilde{g}_{Z1}(m_\chi, \tilde{m}_{f_j}, \tilde{m}_{f_k}, m_{f_i}) + \tilde{C}_{fZ2}^{jki} \tilde{g}_{Z2}(m_\chi, \tilde{m}_{f_j}, \tilde{m}_{f_k}, m_{f_i})], \end{aligned} \quad (61)$$

with

$$C_{fZ1}^{kij} = \frac{1}{2} [C_{fZR}^{ij} C_{f\chi R}^{ik} C_{f\chi R}^{jk*} + C_{fZL}^{ij} C_{f\chi L}^{ik} C_{f\chi L}^{jk*}], \quad (62)$$

$$C_{fZ2}^{kij} = \frac{m_{f_i} m_{f_j}}{2m_\chi^2} [C_{fZR}^{ij} C_{f\chi L}^{ik} C_{f\chi L}^{jk*} + C_{fZL}^{ij} C_{f\chi R}^{ik} C_{f\chi R}^{jk*}], \quad (63)$$

$$\begin{aligned} C_{fZ3}^{kij} = & \frac{1}{2m_\chi} [C_{fZR}^{ij} \{m_{f_i} C_{f\chi L}^{ik} C_{f\chi R}^{jk*} + m_{f_j} C_{f\chi R}^{ik} C_{f\chi L}^{jk*}\} \\ & + C_{fZL}^{ij} \{m_{f_i} C_{f\chi R}^{ik} C_{f\chi L}^{jk*} + m_{f_j} C_{f\chi L}^{ik} C_{f\chi R}^{jk*}\}], \end{aligned} \quad (64)$$

$$\tilde{C}_{fZ1}^{jki} = \frac{1}{2} \tilde{C}_{fZ}^{jk} [C_{f\chi L}^{ik} C_{f\chi L}^{ij*} + C_{f\chi R}^{ik} C_{f\chi R}^{ij*}], \quad (65)$$

$$\tilde{C}_{fZ2}^{jki} = \frac{m_{f_i}}{2m_\chi} \tilde{C}_{fZ}^{jk} [C_{f\chi L}^{ik} C_{f\chi R}^{ij*} + C_{f\chi R}^{ik} C_{f\chi L}^{ij*}], \quad (66)$$

¹²The same diagrams also induce the DM- Z axial-vector couplings. These couplings result in the DM-quark interactions that are velocity-suppressed or spin-dependent, both of which are not considered in our analysis.

and

$$\begin{aligned}
g_{Z1}(m_\chi, M, m_i, m_j) &= -\frac{1}{2}\Delta_{\epsilon,\mu} + \frac{1}{2}\ln M + \frac{m_i^2 \ln m_i - m_j^2 \ln m_j}{2(m_i^2 - m_j^2)} + \frac{m_i^2 + m_j^2 - 2M^2 - m_\chi^2}{2m_\chi^2} \\
&+ \frac{m_i^4 + m_j^4 - m_i^2 m_j^2 - 3M^2(m_i^2 + m_j^2 - M^2) - m_\chi^2(m_i^2 + m_j^2 + 2M^2)}{4m_\chi^4} \ln\left(\frac{M^2}{m_i m_j}\right) \\
&- \frac{1}{4m_\chi^4(m_i^2 - m_j^2)} [2m_\chi^6 - 6m_\chi^4 M^2 + m_\chi^2 \{6M^4 - 2M^2(m_i^2 + m_j^2) - m_i^4 - m_j^4\} \\
&- 2M^6 + 3M^4(m_i^2 + m_j^2) - 3M^2(m_i^4 + m_j^4) + m_i^6 + m_j^6] \ln\left(\frac{m_i}{m_j}\right) \\
&+ \frac{\{(M^2 - m_i^2)^2 + (M^2 - m_\chi^2)^2 - M^4\}\Delta(m_\chi^2, M^2, m_i^2)}{4m_\chi^4(m_i^2 - m_j^2)} L(m_\chi^2, M^2, m_i^2) \\
&- \frac{\{(M^2 - m_j^2)^2 + (M^2 - m_\chi^2)^2 - M^4\}\Delta(m_\chi^2, M^2, m_j^2)}{4m_\chi^4(m_i^2 - m_j^2)} L(m_\chi^2, M^2, m_j^2), \tag{67}
\end{aligned}$$

$$\begin{aligned}
g_{Z2}(m_\chi, M, m_i, m_j) &= \frac{M^2 - m_\chi^2}{m_i^2 - m_j^2} \ln\left(\frac{m_i}{m_j}\right) + \frac{1}{2} \left[\ln\left(\frac{M^2}{m_i m_j}\right) - \frac{m_i^2 + m_j^2}{m_i^2 - m_j^2} \ln\left(\frac{m_i}{m_j}\right) \right] \\
&+ \frac{1}{2(m_i^2 - m_j^2)} [\Delta(m_\chi^2, M^2, m_i^2) L(m_\chi^2, M^2, m_i^2) - \Delta(m_\chi^2, M^2, m_j^2) L(m_\chi^2, M^2, m_j^2)], \tag{68}
\end{aligned}$$

$$\begin{aligned}
g_{Z3}(m_\chi, M, m_i, m_j) &= \frac{1}{2} + \frac{m_i^2 + m_j^2 - 2M^2}{4m_\chi^2} \ln\left(\frac{M^2}{m_i m_j}\right) \\
&- \frac{m_i^4 + m_j^4 - 2M^2(m_i^2 + m_j^2) + 2(M^2 - m_\chi^2)^2}{4m_\chi^2(m_i^2 - m_j^2)} \ln\left(\frac{m_i}{m_j}\right) \\
&+ \frac{(m_i^2 - M^2 + m_\chi^2)\Delta(m_\chi^2, M^2, m_i^2)L(m_\chi^2, M^2, m_i^2) - (m_j^2 - M^2 + m_\chi^2)\Delta(m_\chi^2, M^2, m_j^2)L(m_\chi^2, M^2, m_j^2)}{4m_\chi^2(m_i^2 - m_j^2)}, \tag{69}
\end{aligned}$$

$$\begin{aligned}
\tilde{g}_{Z1}(m_\chi, M_i, M_j, m) &= \frac{1}{2}\Delta_{\epsilon,\mu} - \frac{1}{2}\ln m - \frac{M_i^2 \ln M_i - M_j^2 \ln M_j}{2(M_i^2 - M_j^2)} + \frac{M_i^2 + M_j^2 - 2m^2 + m_\chi^2}{2m_\chi^2} \\
&+ \frac{3m^2(m^2 - M_i^2 - M_j^2) - m_\chi^2(M_i^2 + M_j^2) + M_i^4 + M_j^4 + M_i^2 M_j^2}{4m_\chi^4} \ln\left(\frac{m^2}{M_i M_j}\right) \\
&- \frac{M_i^6 + M_j^6 - (3m^2 + m_\chi^2)(M_i^4 + M_j^4) + 3m^4(M_i^2 + M_j^2) - 2(m^2 - m_\chi^2)^2(m^2 + m_\chi^2)}{4m_\chi^4(M_i^2 - M_j^2)} \ln\left(\frac{M_i}{M_j}\right) \\
&+ \frac{\{(M_i^2 - m^2)^2 - m_\chi^4\}\Delta(m_\chi^2, M_i^2, m^2)L(m_\chi^2, M_i^2, m^2) - \{(M_j^2 - m^2)^2 - m_\chi^4\}\Delta(m_\chi^2, M_j^2, m^2)L(m_\chi^2, M_j^2, m^2)}{4m_\chi^4(M_i^2 - M_j^2)}, \tag{70}
\end{aligned}$$

$$\begin{aligned}
\tilde{g}_{Z2}(m_\chi, M_i, M_j, m) &= -1 - \frac{M_i^2 + M_j^2 - 2m^2}{2m_\chi^2} \ln\left(\frac{m^2}{M_i M_j}\right) \\
&+ \frac{M_i^4 + M_j^4 - 2m^2(M_i^2 + M_j^2) + 2(m^2 - m_\chi^2)^2}{2m_\chi^2(M_i^2 - M_j^2)} \ln\left(\frac{M_i}{M_j}\right) \\
&+ \frac{(m^2 - m_\chi^2 - M_i^2)\Delta(m_\chi^2, M_i^2, m^2)L(m_\chi^2, M_i^2, m^2) - (m^2 - m_\chi^2 - M_j^2)\Delta(m_\chi^2, M_j^2, m^2)L(m_\chi^2, M_j^2, m^2)}{2m_\chi^2(M_i^2 - M_j^2)},
\end{aligned} \tag{71}$$

where $\Delta_{\epsilon,\mu}$ denotes a divergent constant term. This divergent constant does not appear in $C_{\chi Z}$ since

$$\sum_{i,j,k} C_{fZ1}^{kij} = \sum_{i,j,k} \tilde{C}_{fZ1}^{jki} \tag{72}$$

follows from the unitarity of $V_{fL/R}$ and \tilde{V}_f , and thus the divergent terms in g_{Z1} and \tilde{g}_{Z1} cancel with each other. We further note that the effective DM- Z coupling $C_{\chi Z}$ can be generated only after the electroweak symmetry is spontaneously broken; since the DM is singlet under the electroweak gauge symmetry, it can couple to the Z boson only via the electroweak symmetry breaking effects. Diagrammatically, such effects are represented by the insertion of the Higgs VEVs into the diagrams in Fig. 1, and they are represented by effective interactions including the Higgs field with more than dimension six. We have checked that the above expressions are consistent with the result given in Ref. [8].

B.3 DM-Higgs effective interactions

The DM-Higgs effective scalar coupling is induced by the one-loop diagrams shown in Fig. 3. We parametrize the coupling in the broken phase as

$$\mathcal{L}_{\chi h} = \frac{1}{\sqrt{2}} C_{\chi h} \bar{\chi} \chi h. \tag{73}$$

Again, the generation of this coupling requires the electroweak symmetry breaking. It is represented by effective operators including the Higgs field with more than dimension-five. We neglect the pseudo-scalar coupling as it is always suppressed by the DM velocity. The coupling $C_{\chi h}$ is computed as follows:

$$\begin{aligned}
C_{\chi h} &= \frac{1}{(4\pi)^2} \sum_{f,i,j,k} N_c [C_{fh1}^{kij} g_{h1}(m_\chi, \tilde{m}_{f_k}, m_{f_i}, m_{f_j}) \\
&+ C_{fh2}^{kij} g_{h2}(m_\chi, \tilde{m}_{f_k}, m_{f_i}, m_{f_j}) + C_{fh3}^{kij} g_{h3}(m_\chi, \tilde{m}_{f_k}, m_{f_i}, m_{f_j}) \\
&+ \tilde{C}_{fh1}^{jki} \tilde{g}_{h1}(m_\chi, \tilde{m}_{f_j}, \tilde{m}_{f_k}, m_{f_i}) + \tilde{C}_{fh2}^{jki} \tilde{g}_{h2}(m_\chi, \tilde{m}_{f_j}, \tilde{m}_{f_k}, m_{f_i})],
\end{aligned} \tag{74}$$

with

$$C_{fh1}^{kij} = \frac{1}{2} [C_{fhR}^{ij} C_{f\chi L}^{ik} C_{f\chi R}^{jk*} + C_{fhL}^{ij} C_{f\chi R}^{ik} C_{f\chi L}^{jk*}] , \quad (75)$$

$$C_{fh2}^{kij} = \frac{m_{f_i} m_{f_j}}{2m_\chi^2} [C_{fhR}^{ij} C_{f\chi R}^{ik} C_{f\chi L}^{jk*} + C_{fhL}^{ij} C_{f\chi L}^{ik} C_{f\chi R}^{jk*}] , \quad (76)$$

$$C_{fh3}^{kij} = \frac{1}{2m_\chi} [C_{fhR}^{ij} \{m_{f_i} C_{f\chi L}^{ik} C_{f\chi L}^{jk*} + m_{f_j} C_{f\chi R}^{ik} C_{f\chi R}^{jk*}\} \\ + C_{fhL}^{ij} \{m_{f_i} C_{f\chi R}^{ik} C_{f\chi R}^{jk*} + m_{f_j} C_{f\chi L}^{ik} C_{f\chi L}^{jk*}\}] , \quad (77)$$

$$\tilde{C}_{fh1}^{jki} = \frac{1}{2m_\chi} \tilde{C}_{fh}^{jk} [C_{f\chi L}^{ik} C_{f\chi L}^{ij*} + C_{f\chi R}^{ik} C_{f\chi R}^{ij*}] , \quad (78)$$

$$\tilde{C}_{fh2}^{jki} = \frac{m_{f_i}}{2m_\chi^2} \tilde{C}_{fh}^{jk} [C_{f\chi L}^{ik} C_{f\chi R}^{ij*} + C_{f\chi R}^{ik} C_{f\chi L}^{ij*}] , \quad (79)$$

and the mass functions are given by

$$g_{h1}(m_\chi, M, m_i, m_j) = 2 + \Delta_{\epsilon, \mu} - \ln M - \frac{m_i^2 \ln m_i - m_j^2 \ln m_j}{m_i^2 - m_j^2} \\ + \frac{m_i^2 + m_j^2 - M^2}{2m_\chi^2} \ln \left(\frac{M^2}{m_i m_j} \right) - \frac{m_i^4 + m_j^4 - M^2(m_i^2 + m_j^2)}{2m_\chi^2(m_i^2 - m_j^2)} \ln \left(\frac{m_i}{m_j} \right) \\ + \frac{m_i^2 \Delta(m_\chi^2, M^2, m_i^2) L(m_\chi^2, M^2, m_i^2) - m_j^2 \Delta(m_\chi^2, M^2, m_j^2) L(m_\chi^2, M^2, m_j^2)}{2m_\chi^2(m_i^2 - m_j^2)} , \quad (80)$$

$$g_{h2}(m_\chi, M, m_i, m_j) = g_{Z2}(m_\chi, M, m_i, m_j) , \quad (81)$$

$$g_{h3}(m_\chi, M, m_i, m_j) = g_{Z3}(m_\chi, M, m_i, m_j) , \quad (82)$$

$$\tilde{g}_{h1}(m_\chi, M_i, M_j, m) = \frac{1}{2} + \frac{M_i^2 + M_j^2 - 2(m^2 + m_\chi^2)}{4m_\chi^2} \ln \left(\frac{m^2}{M_i M_j} \right) \\ - \frac{M_i^4 + M_j^4 - 2(M_i^2 + M_j^2)(m^2 + m_\chi^2) - 2(m_\chi^4 - m^4)}{4m_\chi^2(M_i^2 - M_j^2)} \ln \left(\frac{M_i}{M_j} \right) \\ + \frac{(M_i^2 - m^2 - m_\chi^2) \Delta(m_\chi^2, M_i^2, m^2) L(m_\chi^2, M_i^2, m^2) - (M_j^2 - m^2 - m_\chi^2) \Delta(m_\chi^2, M_j^2, m^2) L(m_\chi^2, M_j^2, m^2)}{4m_\chi^2(M_i^2 - M_j^2)} , \quad (83)$$

$$\tilde{g}_{h2}(m_\chi, M_i, M_j, m) = -\frac{1}{2} \ln \left(\frac{m^2}{M_i M_j} \right) + \frac{M_i^2 + M_j^2 + 2(m_\chi^2 - m^2)}{2(M_i^2 - M_j^2)} \ln \left(\frac{M_i}{M_j} \right) \\ - \frac{\Delta(m_\chi^2, M_i^2, m^2) L(m_\chi^2, M_i^2, m^2) - \Delta(m_\chi^2, M_j^2, m^2) L(m_\chi^2, M_j^2, m^2)}{2(M_i^2 - M_j^2)} . \quad (84)$$

Again, the divergent constant $\Delta_{\epsilon,\mu}$ in g_{h1} does not contribute to $C_{\chi h}$ since

$$\sum_{i,j,k} C_{fh1}^{kij} = 0. \quad (85)$$

We have checked that the above expressions are consistent with the results given in Refs. [8, 10].

B.4 DM-gluon effective interactions

The diagrams in Fig. 4 give rise to the effective DM-gluon scalar coupling.¹³ At the vector-like fermion mass threshold, the Wilson coefficient of the gluon operator in Eq. (25), $C_S^g(m_{\text{vec}})$, is given by [53]

$$C_S^g(m_{\text{vec}}) = \frac{1}{16} \left[C_{f\chi SS}^{ij} m_\chi \{g_{g1}(m_\chi, \tilde{m}_{f_j}, m_{f_i}) + g_{g2}(m_\chi, \tilde{m}_{f_j}, m_{f_i})\} \right. \\ \left. + \text{Re}[C_{f\chi L}^{ij} C_{f\chi R}^{ij*}] m_{f_i} \{g_{g3}(m_\chi, \tilde{m}_{f_j}, m_{f_i}) + g_{g4}(m_\chi, \tilde{m}_{f_j}, m_{f_i})\} \right], \quad (86)$$

where $C_{f\chi SS}^{ij}$ is defined in Eq. (52) and

$$g_{g1}(m_\chi, M, m) = -\frac{(\Delta - 6M^2 m^2)(M^2 + m^2 - m_\chi^2)}{6\Delta^2 M^2} - \frac{2M^2 m^4}{\Delta^2} L, \quad (87)$$

$$g_{g2}(m_\chi, M, m) = -\frac{\Delta + 12M^2 m^2}{6\Delta^2} + \frac{m^2 M^2 (M^2 + m^2 - m_\chi^2)}{\Delta^2} L, \quad (88)$$

$$g_{g3}(m_\chi, M, m) = -\frac{3\Delta M^2 - (\Delta - 6m^2 M^2)(M^2 - m^2 + m_\chi^2)}{6\Delta^2 M^2} \\ + \frac{m^2 M^2 (M^2 - m^2 - m_\chi^2)}{\Delta^2} L, \quad (89)$$

$$g_{g4}(m_\chi, M, m) = \frac{3\Delta m^2 + 2(\Delta + 3m^2 M^2)(M^2 - m^2 - m_\chi^2)}{6\Delta^2 m^2} \\ - \frac{M^2 \{\Delta + m^2 (M^2 - m^2 + m_\chi^2)\}}{\Delta^2} L. \quad (90)$$

B.5 Low-energy DM-quark/gluon couplings

The DM-quark low-energy effective interactions in Eq. (25) are obtained from the DM- Z and DM-Higgs effective couplings, $C_{\chi Z}$ and $C_{\chi h}$, by integrating out the Z and Higgs boson

¹³It is found to be convenient to compute these diagrams in the Fock-Schwinger gauge [52], where the diagrams (a) and (c) vanish [53], the diagram (b) gives g_{g1} and g_{g3} , and the diagram (d) yields g_{g2} and g_{g4} .

fields, respectively:

$$C_V^q = -\frac{2}{v^2}(T_{3q} - 2Q_q \sin^2 \theta_W)C_{\chi Z} , \quad (91)$$

$$C_S^q = -\frac{1}{\sqrt{2}m_h^2 v}C_{\chi h} , \quad (92)$$

where $T_{3q} = +1/2$ ($-1/2$) and $Q_q = 2/3$ ($-1/3$) for up-type (down-type) quarks, $v \simeq 246$ GeV is the Higgs VEV, θ_W is the weak-mixing angle, and m_h is the Higgs boson mass.

For the DM-gluon low-energy coupling C_S^g , not only the contribution from the diagrams in Fig. 4, $C_S^g(m_{\text{vec}})$, but also those from the DM-heavy quark interactions induced by the Higgs coupling $C_{\chi h}$ should be included. We thus have

$$C_S^g = C_S^g(m_{\text{vec}}) + \frac{1}{4\sqrt{2}m_h^2 v}C_{\chi h} , \quad (93)$$

where the second term in the right-hand side represents the contributions from charm, bottom, and top quarks. These long-distance contributions receive relatively large QCD corrections—for the inclusion of such corrections, see Refs. [36, 54].

C Velocity Integrals

As we see in Sec. 4.3, to obtain the differential event rate we need to perform the following velocity integrals:

$$\zeta(E_R) = \int_{v_{\min}}^{\infty} \frac{d^3\mathbf{v}}{v} f(\mathbf{v} + \mathbf{v}_E) , \quad \xi(E_R) = \int_{v_{\min}}^{\infty} d^3\mathbf{v} v f(\mathbf{v} + \mathbf{v}_E) , \quad (94)$$

with

$$f(\mathbf{v}) = \begin{cases} \frac{1}{N} e^{-v^2/v_0^2} & (|\mathbf{v}| < v_{\text{esc}}) \\ 0 & (|\mathbf{v}| > v_{\text{esc}}) \end{cases} , \quad (95)$$

where

$$N = \pi^{3/2} v_0^3 \left[\text{erf}\left(\frac{v_{\text{esc}}}{v_0}\right) - \frac{2v_{\text{esc}}}{\sqrt{\pi}v_0} e^{-\frac{v_{\text{esc}}^2}{v_0^2}} \right] . \quad (96)$$

With this constant N , the distribution function $f(\mathbf{v})$ is normalized such that

$$\int d^3\mathbf{v} f(\mathbf{v}) = 1 . \quad (97)$$

In what follows, we summarize analytical expressions of the integrals in Eq. (94).

The analytical expression for the integral $\zeta(E_R)$ is given in Refs. [55, 56]:

- For $v_E + v_{\min} < v_{\text{esc}}$,

$$\zeta(E_R) = \frac{\pi^{3/2} v_0^3}{2N v_E} \left[\text{erf}\left(\frac{v_{\min} + v_E}{v_0}\right) - \text{erf}\left(\frac{v_{\min} - v_E}{v_0}\right) - \frac{4v_E}{\sqrt{\pi}v_0} \exp\left(-\frac{v_{\text{esc}}^2}{v_0^2}\right) \right] . \quad (98)$$

- For $v_{\min} > |v_{\text{esc}} - v_{\text{E}}|$ and $v_{\text{E}} + v_{\text{esc}} > v_{\min}$,

$$\zeta(E_R) = \frac{\pi^{3/2} v_0^3}{2N v_{\text{E}}} \left[\operatorname{erf}\left(\frac{v_{\text{esc}}}{v_0}\right) + \operatorname{erf}\left(\frac{v_{\text{E}} - v_{\min}}{v_0}\right) - \frac{2}{\sqrt{\pi}} \left\{ \frac{v_{\text{esc}} + v_{\text{E}} - v_{\min}}{v_0} \right\} e^{-\frac{v_{\text{esc}}^2}{v_0^2}} \right]. \quad (99)$$

- For $v_{\text{E}} > v_{\min} + v_{\text{esc}}$,

$$\zeta(E_R) = \frac{1}{v_{\text{E}}}. \quad (100)$$

- For $v_{\text{E}} + v_{\text{esc}} < v_{\min}$,

$$\zeta(E_R) = 0. \quad (101)$$

An analytical expression for $\xi(E_R)$ is given as follows:

- For $v_{\text{E}} + v_{\min} < v_{\text{esc}}$,

$$\begin{aligned} \xi(E_R) = & \frac{\pi^{3/2} v_0^5}{4N v_{\text{E}}} \left[\frac{v_0^2 + 2v_{\text{E}}^2}{v_0^2} \left\{ \operatorname{erf}\left(\frac{v_{\min} + v_{\text{E}}}{v_0}\right) - \operatorname{erf}\left(\frac{v_{\min} - v_{\text{E}}}{v_0}\right) \right\} - \frac{8v_{\text{E}}}{\sqrt{\pi} v_0} e^{-\frac{v_{\text{esc}}^2}{v_0^2}} \right. \\ & + \frac{2}{\sqrt{\pi}} \left\{ \frac{v_{\min} + v_{\text{E}}}{v_0} e^{-\frac{(v_{\min} - v_{\text{E}})^2}{v_0^2}} - \frac{v_{\min} - v_{\text{E}}}{v_0} e^{-\frac{(v_{\min} + v_{\text{E}})^2}{v_0^2}} \right\} \\ & \left. + \frac{4}{3\sqrt{\pi}} \left\{ \frac{(v_{\text{esc}} - v_{\text{E}})^3 - (v_{\text{esc}} + v_{\text{E}})^3}{v_0^3} \right\} e^{-\frac{v_{\text{esc}}^2}{v_0^2}} \right]. \quad (102) \end{aligned}$$

- For $v_{\min} > |v_{\text{esc}} - v_{\text{E}}|$ and $v_{\text{E}} + v_{\text{esc}} > v_{\min}$,

$$\begin{aligned} \xi(E_R) = & \frac{\pi^{3/2} v_0^5}{4N v_{\text{E}}} \left[\frac{v_0^2 + 2v_{\text{E}}^2}{v_0^2} \left\{ \operatorname{erf}\left(\frac{v_{\text{esc}}}{v_0}\right) - \operatorname{erf}\left(\frac{v_{\min} - v_{\text{E}}}{v_0}\right) \right\} \right. \\ & + \frac{2}{\sqrt{\pi}} \left\{ \frac{v_{\min} + v_{\text{E}}}{v_0} e^{-\frac{(v_{\min} - v_{\text{E}})^2}{v_0^2}} - \frac{v_{\text{esc}} + 2v_{\text{E}}}{v_0} e^{-\frac{v_{\text{esc}}^2}{v_0^2}} \right\} \\ & \left. + \frac{4}{3\sqrt{\pi}} \left\{ \frac{v_{\min}^3 - (v_{\text{esc}} + v_{\text{E}})^3}{v_0^3} \right\} e^{-\frac{v_{\text{esc}}^2}{v_0^2}} \right]. \quad (103) \end{aligned}$$

- For $v_{\text{E}} > v_{\min} + v_{\text{esc}}$,

$$\xi(E_R) = v_{\text{E}} + \frac{v_0^2}{2v_{\text{E}}} - \frac{2\pi v_0^2 v_{\text{esc}}^3}{3N v_{\text{E}}} e^{-\frac{v_{\text{esc}}^2}{v_0^2}}. \quad (104)$$

- For $v_{\text{E}} + v_{\text{esc}} < v_{\min}$,

$$\xi(E_R) = 0. \quad (105)$$

We have checked that these results are consistent with those given in Ref. [57].

D Direct Detection Limits/Prospects

In this section, we show our prescription for the estimate of the current limit and future prospects of the direct detection experiments. For the current bound, we use the latest result from the XENON1T experiment [40], while for a future experiment, we consider XENONnT [41]. We have checked that the sensitivity of the LZ experiment [42] is as good as that of XENONnT.

Recently, the XENON1T collaboration reported their latest result of DM direct search based on data with an exposure $w_{\text{exp}} = 278.8 \text{ days} \times 1.30(1) \text{ ton}$. The expected number of DM-nuclei scattering events in this experiment is estimated as follows [58]:

$$N_{\text{event}} = w_{\text{exp}} \int_{S_1^{\text{min}}}^{S_1^{\text{max}}} dS_1 \sum_{n=1}^{\infty} \text{Gauss}(S_1|n, \sqrt{n}\sigma_{\text{PMT}}) \int_0^{\infty} dE_R \epsilon(E_R) \text{Poiss}(n|\nu(E_R)) \frac{dR}{dE_R}, \quad (106)$$

where $S_1^{\text{min}} = 3$ photoelectrons (PE), $S_1^{\text{max}} = 70$ PE, σ_{PMT} is the average single-PE resolution of the photomultipliers, $\epsilon(E_R)$ is the detection efficiency, and $\nu(E_R)$ is the expected number of PEs for a given recoil energy E_R . We conservatively take $\sigma_{\text{PMT}} = 0.4$ [59, 60], and read $\epsilon(E_R)$ from the black solid line in Fig. 1 in Ref. [40]. We obtain $\nu(E_R)$ from the S1 yield given in the lower left panel in Fig. 13 in Ref. [41], which corresponds to $\nu(E_R)/E_R$.¹⁴

To derive a bound from XENON1T, we consider the following Test Statistic as in Ref. [62]:

$$\text{TS}(m_\chi) = -2 \ln \left[\frac{\mathcal{L}(N_{\text{event}})}{\mathcal{L}_{\text{BG}}} \right], \quad (108)$$

with

$$\mathcal{L}(N_{\text{event}}) = \frac{1}{N_{\text{obs}}!} (N_{\text{event}} + N_{\text{BG}})^{N_{\text{obs}}} \exp\{-(N_{\text{event}} + N_{\text{BG}})\}, \quad (109)$$

where N_{obs} and N_{BG} are the numbers of the observed and background events, respectively, and $\mathcal{L}_{\text{BG}} \equiv \mathcal{L}(0)$. We obtain 90% CL limits from the condition $\text{TS}(m_\chi) > 2.71$, with $N_{\text{obs}} = 14$ and $N_{\text{BG}} = 7.36(61)$ [40], which corresponds to $N_{\text{event}} \lesssim 19.5$. We have checked that the bound obtained in this way is more conservative than the XENON1T limit [40] by a factor of ~ 2 .

To assess the future prospects, we consider XENONnT with an exposure $w_{\text{exp}} = 20 \text{ t} \cdot \text{yrs}$. We then apply the maximum gap method [63] on the assumption of zero observed events, following Ref. [64]; namely, we require $1 - \exp(-N_{\text{event}}) \geq 0.9$, which corresponds to $N_{\text{event}} \lesssim 2.3$.

¹⁴We can also estimate $\nu(E_R)$ using

$$\nu(E_R) = E_R \cdot \mathcal{L}_{\text{eff}} \cdot \mathcal{L}_y \cdot S_{\text{NR}}, \quad (107)$$

where $S_{\text{NR}} = 0.95$ is the light yield suppression factor for nuclear recoils due to the electric field, $\mathcal{L}_y = 7.7 \text{ PE/keV}$ [41] is the average light yield, and \mathcal{L}_{eff} is the relative scintillation efficiency given in Ref. [61]. We have checked that $\nu(E_R)$ obtained in this manner is in a good agreement with that estimated from the S1 yield.

E Electric Dipole Moments

In this section, we summarize the analytical expressions used in the calculation of the nucleon and electron EDMs.

E.1 Weinberg operator

The Wilson coefficient of the Weinberg operator in Eq. (38) is obtained by computing the diagram in Fig. 8:

$$w = -\frac{3g_s^3}{2(4\pi)^4} \sum_{f=u,d} \sum_{i,j} m_\chi m_{f_i} \text{Im} [C_{f\chi L}^{ij} C_{f\chi R}^{ij*}] f_1(m_\chi^2, m_{f_i}^2, \tilde{m}_{f_j}^2), \quad (110)$$

where the mass function $f_1(m_\chi^2, m_{f_i}^2, \tilde{m}_{f_j}^2)$ is given in Eq. (3.28) in Ref. [43]. The analytic expression of $f_1(m_\chi^2, m_{f_i}^2, \tilde{m}_{f_j}^2)$ is obtained as

$$f_1(m_\chi^2, m_{f_i}^2, \tilde{m}_{f_j}^2) = -\left\{ \frac{1}{3} \left(\frac{\partial}{\partial m_\chi^2} \right)^3 + \frac{m_\chi^2}{6} \left(\frac{\partial}{\partial m_\chi^2} \right)^4 \right\} I(m_\chi^2, \tilde{m}_{f_j}^2, m_{f_i}^2), \quad (111)$$

where $I(m_\chi^2, \tilde{m}_{f_j}^2, m_{f_i}^2)$ is given in Eq. (2.19) in Ref. [65]. Note that the above expression contains the same factor as that in Eq. (50): $\text{Im}[C_{f\chi L}^{ij} C_{f\chi R}^{ij*}]$.

E.2 Barr-Zee-type contribution

The electron EDM induced by the Barr-Zee diagrams in Fig. 10 is given by

$$d_e = d_e^{h\gamma} + d_e^{hZ} + d_e^{WW}, \quad (112)$$

with

$$d_e^{h\gamma} = -\frac{8N_c y_e e^3}{(4\pi)^4 m_h^2} \sum_{f,i} Q_f^2 m_{f_i} \text{Im}[C_{fhR}^{ii}] f_{\text{BZ}} \left(0, \frac{m_{f_i}^2}{m_h^2}, \frac{m_{f_i}^2}{m_h^2} \right), \quad (113)$$

$$d_e^{hZ} = -\frac{4N_c y_e g_Z^2 e}{(4\pi)^4 m_h^2} \left(-\frac{1}{2} + 2 \sin^2 \theta_W \right) \times \sum_{f,i,j} Q_f m_{f_i} \text{Im}[(C_{fZR}^{ji} C_{fhR}^{ij} - C_{fZL}^{ji} C_{fhL}^{ij})] f_{\text{BZ}} \left(\frac{m_Z^2}{m_h^2}, \frac{m_{f_i}^2}{m_h^2}, \frac{m_{f_j}^2}{m_h^2} \right), \quad (114)$$

$$d_e^{WW} = -\frac{3g^2 e}{(4\pi)^4} \frac{m_e}{m_W^4} \sum_{i,j} m_{u_i} m_{d_j} \left[Q_u \text{Im}[C_{QWL}^{ij*} C_{QWR}^{ij}] f_{\text{BZ}} \left(0, \frac{m_{d_j}^2}{m_W^2}, \frac{m_{u_i}^2}{m_W^2} \right) + Q_d \text{Im}[C_{QWL}^{ji*} C_{QWR}^{ji}] f_{\text{BZ}} \left(0, \frac{m_{u_i}^2}{m_W^2}, \frac{m_{d_j}^2}{m_W^2} \right) \right], \quad (115)$$

for model I and

$$d_e^{WW} = -\frac{g^2 e}{(4\pi)^4} \frac{m_e}{m_W^4} \sum_i m_\nu m_{e_i} \left[Q_e \text{Im}[C_{LWL}^{i*} C_{LWR}^i] f_{\text{BZ}} \left(0, \frac{m_\nu^2}{m_W^2}, \frac{m_{e_i}^2}{m_W^2} \right) \right],$$

for model II, where the mass function is given by

$$f_{\text{BZ}}(r, r_1, r_2) = \int_0^1 dx \frac{1}{1-x} j \left(r, \frac{xr_1 + (1-x)r_2}{x(1-x)} \right), \quad (116)$$

$$j(r, s) = \frac{1}{r-s} \left(\frac{r \ln r}{r-1} - \frac{s \ln s}{s-1} \right). \quad (117)$$

Here, m_h , m_Z , and m_W are the Higgs, Z , and W boson masses, respectively, and m_e ($\equiv y_e v / \sqrt{2}$) is the electron mass.

In Model I, the CEDM for quark q

$$\mathcal{L} = -\frac{i}{2} g_s \tilde{d}_q \bar{q} G_{\mu\nu}^A \sigma^{\mu\nu} T^A \gamma_5 q, \quad (118)$$

is also generated from the upper left diagram in Fig. 10 with the γ/Z lines replaced with gluon lines. The resultant expression is given by

$$\tilde{d}_q = -\frac{32 g_s^2 y_q}{3(4\pi)^4 m_h^2} \sum_{f,i} m_{f_i} \text{Im}[C_{fhR}^{ii}] f_{\text{BZ}} \left(0, \frac{m_{f_i}^2}{m_h^2}, \frac{m_{f_i}^2}{m_h^2} \right). \quad (119)$$

where the quark Yukawa coupling constant y_q is given as $m_q = y_q v / \sqrt{2}$ (m_q : quark mass).

References

- [1] G. Arcadi, M. Dutra, P. Ghosh, M. Lindner, Y. Mambrini, M. Pierre, S. Profumo, and F. S. Queiroz, *Eur. Phys. J.* **C78**, 203 (2018), arXiv:1703.07364 [hep-ph].
- [2] V. Silveira and A. Zee, *Phys. Lett.* **B161**, 136 (1985); J. McDonald, *Phys. Rev.* **D50**, 3637 (1994), arXiv:hep-ph/0702143 [hep-ph]; C. P. Burgess, M. Pospelov, and T. ter Veldhuis, *Nucl. Phys.* **B619**, 709 (2001), arXiv:hep-ph/0011335 [hep-ph]; H. Davoudiasl, R. Kitano, T. Li, and H. Murayama, *Phys. Lett.* **B609**, 117 (2005), arXiv:hep-ph/0405097 [hep-ph].
- [3] P. Hut and K. A. Olive, *Phys. Lett.* **B87**, 144 (1979); S. Nussinov, *Phys. Lett.* **B165**, 55 (1985); S. M. Barr, R. S. Chivukula, and E. Farhi, *Phys. Lett.* **B241**, 387 (1990); S. M. Barr, *Phys. Rev.* **D44**, 3062 (1991); D. B. Kaplan, *Phys. Rev. Lett.* **68**, 741 (1992); S. Dodelson, B. R. Greene, and L. M. Widrow, *Nucl. Phys.* **B372**, 467 (1992); V. A. Kuzmin, *Nonaccelerator new physics. Proceedings, 1st International Workshop, NANP'97, Dubna, Russia, July 7-11, 1997*, *Phys. Part. Nucl.* **29**, 257 (1998), [*Phys. Atom. Nucl.* 61,1107(1998)], arXiv:hep-ph/9701269 [hep-ph]; D. Hooper, J. March-Russell, and S. M. West, *Phys. Lett.* **B605**, 228 (2005), arXiv:hep-ph/0410114 [hep-ph]; R. Kitano and I. Low, *Phys. Rev.* **D71**, 023510 (2005), arXiv:hep-ph/0411133 [hep-ph]; G. R. Farrar and G. Zaharijas, *Phys. Rev. Lett.* **96**, 041302 (2006), arXiv:hep-ph/0510079 [hep-ph]; D. E. Kaplan, M. A. Luty, and K. M. Zurek, *Phys. Rev.* **D79**, 115016 (2009), arXiv:0901.4117 [hep-ph]; N. Nagata, K. A. Olive, and J. Zheng, *JCAP* **1702**, 016 (2017), arXiv:1611.04693 [hep-ph].
- [4] Y. G. Kim, K. Y. Lee, and S. Shin, *JHEP* **05**, 100 (2008), arXiv:0803.2932 [hep-ph]; S. Kanemura, O. Seto, and T. Shimomura, *Phys. Rev.* **D84**, 016004 (2011), arXiv:1101.5713 [hep-ph]; M. Lindner, D. Schmidt, and T. Schwetz, *Phys. Lett.* **B705**, 324 (2011), arXiv:1105.4626 [hep-ph]; S. Kanemura, T. Nabeshima, and H. Sugiyama, *Phys. Rev.* **D85**, 033004 (2012), arXiv:1111.0599 [hep-ph]; S. Baek, P. Ko, and W.-I. Park, *JHEP* **02**, 047 (2012), arXiv:1112.1847 [hep-ph]; P. Ko, N. Nagata, and Y. Tang, *Phys. Lett.* **B773**, 513 (2017), arXiv:1706.05605 [hep-ph].
- [5] N. Okada and O. Seto, *Phys. Rev.* **D82**, 023507 (2010), arXiv:1002.2525 [hep-ph].
- [6] K. Cheung and T.-C. Yuan, *JHEP* **03**, 120 (2007), arXiv:hep-ph/0701107 [hep-ph]; Y. Mambrini, *JCAP* **1107**, 009 (2011), arXiv:1104.4799 [hep-ph]; H. An, X. Ji, and L.-T. Wang, *JHEP* **07**, 182 (2012), arXiv:1202.2894 [hep-ph]; V. Barger, D. Marfatia, and A. Peterson, *Phys. Rev.* **D87**, 015026 (2013), arXiv:1206.6649 [hep-ph]; X. Chu, Y. Mambrini, J. Quevillon, and B. Zaldivar, *JCAP* **1401**, 034 (2014), arXiv:1306.4677 [hep-ph]; G. Arcadi, Y. Mambrini, M. H. G. Tytgat, and B. Zaldivar, *JHEP* **03**, 134 (2014), arXiv:1401.0221 [hep-ph]; O. Lebedev and Y. Mambrini, *Phys. Lett.* **B734**, 350 (2014), arXiv:1403.4837 [hep-ph]; Y. Mambrini, S. Profumo, and F. S. Queiroz, *Phys. Lett.* **B760**, 807 (2016), arXiv:1508.06635 [hep-ph].
- [7] P. Agrawal, S. Blanchet, Z. Chacko, and C. Kilic, *Phys. Rev.* **D86**, 055002 (2012), arXiv:1109.3516 [hep-ph]; N. Weiner and I. Yavin, *Phys. Rev.* **D87**, 023523 (2013), arXiv:1209.1093 [hep-ph]; Y. Bai and J. Berger, *JHEP* **11**, 171 (2013), arXiv:1308.0612 [hep-ph]; A. DiFranzo, K. I. Nagao, A. Rajaraman, and T. M. P. Tait, *JHEP* **11**, 014

- (2013), [Erratum: JHEP01,162(2014)], arXiv:1308.2679 [hep-ph]; J. Kopp, L. Michaels, and J. Smirnov, JCAP **1404**, 022 (2014), arXiv:1401.6457 [hep-ph]; Y. Bai and J. Berger, JHEP **08**, 153 (2014), arXiv:1402.6696 [hep-ph]; S. Chang, R. Edezhath, J. Hutchinson, and M. Luty, Phys. Rev. **D90**, 015011 (2014), arXiv:1402.7358 [hep-ph]; P. Agrawal, Z. Chacko, and C. B. Verhaaren, JHEP **08**, 147 (2014), arXiv:1402.7369 [hep-ph]; P. Agrawal, B. Batell, D. Hooper, and T. Lin, Phys. Rev. **D90**, 063512 (2014), arXiv:1404.1373 [hep-ph]; A. Hamze, C. Kilic, J. Koeller, C. Trendafilova, and J.-H. Yu, Phys. Rev. **D91**, 035009 (2015), arXiv:1410.3030 [hep-ph]; Z.-H. Yu, X.-J. Bi, Q.-S. Yan, and P.-F. Yin, Phys. Rev. **D91**, 035008 (2015), arXiv:1410.3347 [hep-ph]; C. Kilic, M. D. Klimek, and J.-H. Yu, Phys. Rev. **D91**, 054036 (2015), arXiv:1501.02202 [hep-ph]; R. Primulando, E. Salvioni, and Y. Tsai, JHEP **07**, 031 (2015), arXiv:1503.04204 [hep-ph]; P. Ko, A. Natale, M. Park, and H. Yokoya, JHEP **01**, 086 (2017), arXiv:1605.07058 [hep-ph]; W. Chao, H.-K. Guo, and H.-L. Li, JCAP **1702**, 002 (2017), arXiv:1606.07174 [hep-ph].
- [8] A. Ibarra and S. Wild, JCAP **1505**, 047 (2015), arXiv:1503.03382 [hep-ph].
- [9] M. J. Baker and A. Thamm, (2018), arXiv:1806.07896 [hep-ph].
- [10] J. Herrero-Garcia, E. Molinaro, and M. A. Schmidt, Eur. Phys. J. **C78**, 471 (2018), arXiv:1803.05660 [hep-ph].
- [11] T. Banks, J.-F. Fortin, and S. Thomas, (2010), arXiv:1007.5515 [hep-ph].
- [12] S. Weinberg, Phys. Rev. Lett. **63**, 2333 (1989).
- [13] F. J. Botella, G. C. Branco, and M. Nebot, JHEP **12**, 040 (2012), arXiv:1207.4440 [hep-ph].
- [14] A. K. Alok, S. Banerjee, D. Kumar, and S. Uma Sankar, Nucl. Phys. **B906**, 321 (2016), arXiv:1402.1023 [hep-ph].
- [15] C. Bobeth, A. J. Buras, A. Celis, and M. Jung, JHEP **04**, 079 (2017), arXiv:1609.04783 [hep-ph].
- [16] T. Morozumi, Y. Shimizu, S. Takahashi, and H. Umeeda, PTEP **2018**, 043B10 (2018), arXiv:1801.05268 [hep-ph].
- [17] N. Aghanim *et al.* (Planck), (2018), arXiv:1807.06209 [astro-ph.CO].
- [18] K. Griest and D. Seckel, Phys. Rev. **D43**, 3191 (1991).
- [19] J. Hisano, S. Matsumoto, and M. M. Nojiri, Phys. Rev. Lett. **92**, 031303 (2004), arXiv:hep-ph/0307216 [hep-ph].
- [20] J. Hisano, S. Matsumoto, M. M. Nojiri, and O. Saito, Phys. Rev. **D71**, 063528 (2005), arXiv:hep-ph/0412403 [hep-ph].
- [21] J. Hisano, S. Matsumoto, M. Nagai, O. Saito, and M. Senami, Phys. Lett. **B646**, 34 (2007), arXiv:hep-ph/0610249 [hep-ph].

- [22] J. Ellis, F. Luo, and K. A. Olive, *JHEP* **09**, 127 (2015), arXiv:1503.07142 [hep-ph].
- [23] S. P. Liew and F. Luo, *JHEP* **02**, 091 (2017), arXiv:1611.08133 [hep-ph].
- [24] *Combination of the searches for pair-produced vector-like partners of the third generation quarks at $\sqrt{s} = 13$ TeV with the ATLAS detector*, Tech. Rep. ATLAS-CONF-2018-032 (CERN, Geneva, 2018).
- [25] A. M. Sirunyan *et al.* (CMS), (2018), 10.3204/PUBDB-2018-02202, arXiv:1805.04758 [hep-ex].
- [26] G. Aad *et al.* (ATLAS), *Phys. Rev.* **D92**, 112007 (2015), arXiv:1509.04261 [hep-ex].
- [27] A. M. Sirunyan *et al.* (CMS), *Phys. Rev.* **D97**, 072008 (2018), arXiv:1708.02510 [hep-ex].
- [28] M. Aaboud *et al.* (ATLAS), *Phys. Rev.* **D97**, 112001 (2018), arXiv:1712.02332 [hep-ex].
- [29] A. M. Sirunyan *et al.* (CMS), *Phys. Rev.* **D96**, 032003 (2017), arXiv:1704.07781 [hep-ex].
- [30] J. Hisano, R. Nagai, and N. Nagata, *JHEP* **05**, 037 (2015), arXiv:1502.02244 [hep-ph].
- [31] J. Hisano, K. Ishiwata, and N. Nagata, *JHEP* **06**, 097 (2015), arXiv:1504.00915 [hep-ph].
- [32] A. Crivellin, F. D’Eramo, and M. Procura, *Phys. Rev. Lett.* **112**, 191304 (2014), arXiv:1402.1173 [hep-ph].
- [33] F. D’Eramo and M. Procura, *JHEP* **04**, 054 (2015), arXiv:1411.3342 [hep-ph].
- [34] J. Brod, B. Grinstein, E. Stamou, and J. Zupan, *JHEP* **02**, 174 (2018), arXiv:1801.04240 [hep-ph].
- [35] F. Bishara, J. Brod, B. Grinstein, and J. Zupan, (2018), arXiv:1809.03506 [hep-ph].
- [36] J. Ellis, N. Nagata, and K. A. Olive, *Eur. Phys. J.* **C78**, 569 (2018), arXiv:1805.09795 [hep-ph].
- [37] M. A. Shifman, A. I. Vainshtein, and V. I. Zakharov, *Phys. Lett.* **78B**, 443 (1978).
- [38] J. D. Lewin and P. F. Smith, *Astropart. Phys.* **6**, 87 (1996).
- [39] R. H. Helm, *Phys. Rev.* **104**, 1466 (1956).
- [40] E. Aprile *et al.* (XENON), (2018), arXiv:1805.12562 [astro-ph.CO].
- [41] E. Aprile *et al.* (XENON), *JCAP* **1604**, 027 (2016), arXiv:1512.07501 [physics.ins-det].
- [42] D. S. Akerib *et al.* (LUX-ZEPLIN), (2018), arXiv:1802.06039 [astro-ph.IM].
- [43] T. Abe, J. Hisano, and R. Nagai, *JHEP* **03**, 175 (2018), arXiv:1712.09503 [hep-ph].
- [44] D. A. Demir, M. Pospelov, and A. Ritz, *Phys. Rev.* **D67**, 015007 (2003), arXiv:hep-ph/0208257 [hep-ph].

- [45] G. Degrassi, E. Franco, S. Marchetti, and L. Silvestrini, *JHEP* **11**, 044 (2005), arXiv:hep-ph/0510137 [hep-ph].
- [46] C. A. Baker *et al.*, *Phys. Rev. Lett.* **97**, 131801 (2006), arXiv:hep-ex/0602020 [hep-ex].
- [47] A. Lehrach, B. Lorentz, W. Morse, N. Nikolaev, and F. Rathmann, (2012), arXiv:1201.5773 [hep-ex].
- [48] J. Baron *et al.* (ACME), *Science* **343**, 269 (2014), arXiv:1310.7534 [physics.atom-ph].
- [49] D. M. Kara, I. J. Smallman, J. J. Hudson, B. E. Sauer, M. R. Tarbutt, and E. A. Hinds, *New Journal of Physics* **14**, 103051 (2012), arXiv:1208.4507 [physics.atom-ph].
- [50] D. Kawall, *Spin physics. Proceedings, 19th International Symposium, SPIN 2010, Juelich, Germany, September 27-October 2, 2010*, *J. Phys. Conf. Ser.* **295**, 012031 (2011).
- [51] S. M. Barr and A. Zee, *Phys. Rev. Lett.* **65**, 21 (1990), [Erratum: *Phys. Rev. Lett.* 65,2920(1990)].
- [52] V. Fock, *Phys. Z. Sowjetunion* **12**, 404 (1937); J. S. Schwinger, *PARTICLES, SOURCES AND FIELDS. VOLUME II* (1973); C. Cronstrom, *Phys. Lett.* **90B**, 267 (1980); V. A. Novikov, M. A. Shifman, A. I. Vainshtein, and V. I. Zakharov, *Fortsch. Phys.* **32**, 585 (1984).
- [53] J. Hisano, K. Ishiwata, and N. Nagata, *Phys. Rev.* **D82**, 115007 (2010), arXiv:1007.2601 [hep-ph].
- [54] L. Vecchi, (2013), arXiv:1312.5695 [hep-ph].
- [55] C. Savage, K. Freese, and P. Gondolo, *Phys. Rev.* **D74**, 043531 (2006), arXiv:astro-ph/0607121 [astro-ph].
- [56] C. McCabe, *Phys. Rev.* **D82**, 023530 (2010), arXiv:1005.0579 [hep-ph].
- [57] V. Barger, W.-Y. Keung, and D. Marfatia, *Phys. Lett.* **B696**, 74 (2011), arXiv:1007.4345 [hep-ph].
- [58] E. Aprile *et al.* (XENON100), *Phys. Rev.* **D84**, 052003 (2011), arXiv:1103.0303 [hep-ex].
- [59] E. Aprile *et al.* (XENON), *Eur. Phys. J.* **C75**, 546 (2015), arXiv:1503.07698 [astro-ph.IM].
- [60] P. Barrow *et al.*, *JINST* **12**, P01024 (2017), arXiv:1609.01654 [astro-ph.IM].
- [61] E. Aprile *et al.* (XENON100), *Phys. Rev. Lett.* **107**, 131302 (2011), arXiv:1104.2549 [astro-ph.CO].
- [62] M. Cirelli, E. Del Nobile, and P. Panci, *JCAP* **1310**, 019 (2013), arXiv:1307.5955 [hep-ph].
- [63] S. Yellin, *Phys. Rev. D* **66**, 032005 (2002).
- [64] S. J. Witte and G. B. Gelmini, *JCAP* **1705**, 026 (2017), arXiv:1703.06892 [hep-ph].
- [65] S. P. Martin, *Phys. Rev.* **D65**, 116003 (2002), arXiv:hep-ph/0111209 [hep-ph].